Climate Dynamics (2022) 58:3297–3315
https://doi.org/10.1007/s00382-021-06099-8

Mixed layer heat budget in the eastern equatorial Indian Ocean during the two consecutive positive Indian Ocean dipole events in 2018 and 2019

A. R. Aparna[1,2] · M. S. Girishkumar[2]

Received: 2 July 2021 / Accepted: 5 December 2021 / Published online: 19 January 2022
© The Author(s), under exclusive licence to Springer-Verlag GmbH Germany, part of Springer Nature 2021

Abstract

The Indian Ocean hosted a strong positive Indian Ocean Dipole (pIOD) event in 2019–2020, and a weak event in 2018–2019, such as the magnitude of the cold sea surface temperature anomaly (SSTA) during June-December in the former case is a factor of two higher (~ − 1.5 °C) than the latter (~ − 0.75 °C) at the western periphery of the eastern IOD zone at 5° S, 95° E. The plausible mechanisms responsible for this difference in the SSTA between these two events are examined using the mixed layer heat budget estimate using the moored buoy measurements. It is found that the enhanced cooling during June-December in 2019–2020 is determined primarily by the anomalous cooling due to the vertical processes associated with the combined effect of the anomalous thin barrier layer (BL), shallow thermocline, weak near-surface stratification, and strong wind speed induced vertical mixing, and secondarily by the enhancement in the latent heat flux (*LHF*) loss from the ocean. Conversely, the magnitude of cooling due to the vertical processes is much smaller in 2018–2019 due to the near-climatological states such as a thick BL, deep thermocline, and weak wind speed. During these events, the warming tendency by the horizontal advection dampens the cooling tendency associated with the vertical processes and *LHF*. These characteristics are distinct from the past study that suggested that the horizontal advection was responsible for the cool SSTA at the exact location during an extreme pIOD event in 2006–2007.

1 Introduction

The Indian Ocean Dipole (IOD) event is one of the dominant interannual coupled ocean–atmosphere phenomena in the Indian Ocean (Saji et al. 1999; Webster et al. 1999). The positive phase of the IOD (pIOD) is characterized by the cool sea surface temperature (SST) anomaly (SSTA) and suppressed convective activity in the eastern Equatorial Indian Ocean (EIO, 10° S–Equator and 90° E–110° E), and an anomalous warm SST and enhanced convective activity in the western EIO (50° E–70° E and 10° S–10° N) (Fig. 1c); roughly an opposite situation exists in the EIO during the negative phase of the IOD (nIOD) (Saji et al. 1999; Webster et al. 1999; Horii et al. 2009; Mareta et al. 2018; Zhang et al. 2018a, b; Wang and Cai 2020).

Past studies have demonstrated that an IOD event has the potential to modulate the climatic conditions over the Indian Ocean region (Saji et al. 1999; Webster et al. 1999; Behera et al. 1999; Ashok et al. 2001, 2004; Gadgil et al. 2004; Ajayamohan and Rao 2008; Vinayachandran et al. 2009; Girishkumar et al. 2011; Girishkumar and Ravichandran 2012). For example, past studies have depicted the enhancement of precipitation in the northern Bay of Bengal during the pIOD years (Behera et al. 1999; Ashok et al. 2001; Ajayamohan and Rao 2008). In addition, it has also been shown that pIOD events significantly modulate the tropical cyclone activity in the northern Indian Ocean (Girishkumar and Ravichandran 2012). Besides, previous studies have also demonstrated that the IOD events can significantly modulate the physical and biogeochemical states in the Indian Ocean (Murtugudde et al. 1999; Vinayachandran and Mathew 2003; Pant et al. 2015; Girishkumar et al. 2011). Moreover, IOD events can significantly modulate global climatic conditions through teleconnections (Saji and Yamagata 2003; Behera and Yamagata 2003; Schott et al. 2009; Jiang et al.

✉ M. S. Girishkumar
girish@incois.gov.in

[1] Department of Physical Oceanography, Cochin University of Science and Technology, Cochin, Kerala 682 016, India

[2] Ministry of Earth Sciences (MoES), Indian National Centre for Ocean Information Services (INCOIS), Telangana, Hyderabad 500 055, India

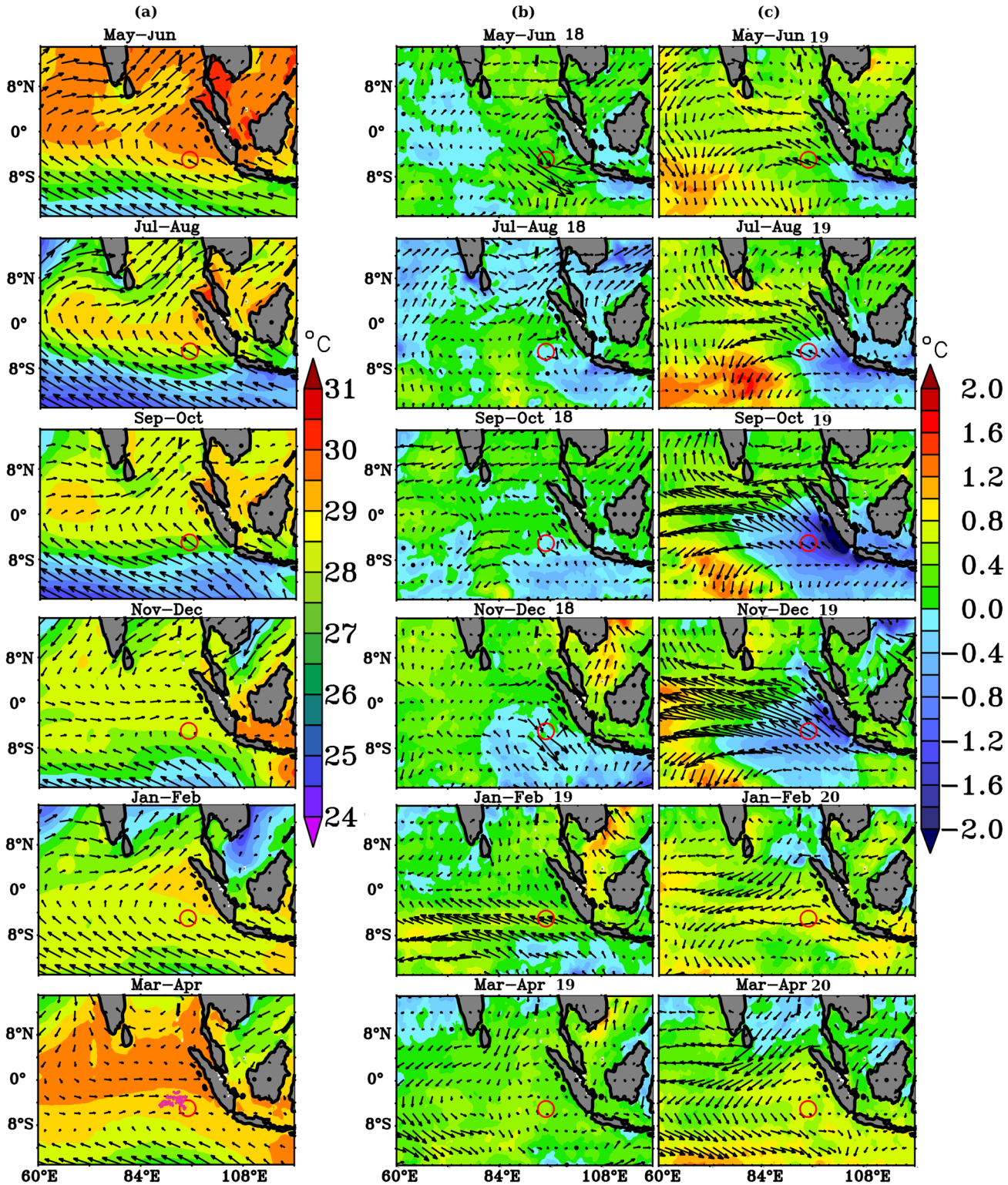

Fig. 1 Spatio-temporal evolution of bi-monthly average of the SST (°C) and wind vectors (m s^{-1}). **a** Climatology (2002–2020) and anomaly during the pIOD events in **b** 2018–2019 and **c** 2019–2020. The red open circles in panels (**a**), (**b**) and (**c**) represent the RAMA mooring location at 5° S, 95° E. The profiling locations of Argo float (WMO ID 2902149) from 1 May 2018 to 1 January 2021 in the south-eastern equatorial Indian Ocean are marked as the pink dots in the bottom panel of (**a**)

2019; Izumo et al. 2010; Wang and Cai 2020). These studies suggest that a better understanding of the factors that modulate the SST in the eastern and western EIO facilitate a better representation of the lifecycle of IOD events in the coupled model using for the seasonal, extended, and future climate predictions. Note that the SST in the eastern EIO remained higher than 27 °C throughout the year (Fig. 1a). Considering the high mean SST in the eastern EIO, even a small SSTA of a magnitude of 0.5 °C in this region can significantly modulate the atmospheric circulation, as demonstrated in previous studies (Palmer and Mansfield 1984). Hence, understanding the factors modulating the interannual SST in the eastern IOD zone have scientific and societal implications.

Dipole Mode Index (DMI) is the most commonly used indices to classify the intensity of an IOD event, and it is defined as the difference in the SSTA between the western EIO (50° E–70° E and 10° S–10° N) and eastern EIO (10° S—Equator and 90° E–110 °E) zone (Saji et al. 1999). The evolution of an IOD event is phase-locked to the seasonal cycle, such as a specific event that develops during late boreal spring (May) or early part of the northern summer (June) and reaches peak intensity during boreal fall (October–November) and decay rapidly after that (Saji et al. 1999; Webster et al. 1999) (Fig. 2a).

The analysis of the DMI data during the last 19 years (2002–2020) showed that the Indian Ocean hosted an extreme pIOD event in 2019–2020 and a relatively weak event in 2018–2019. The DMI magnitude associated with the event in 2019–2020 reached as large as ~ 2.5 °C, which is approximately a factor of two higher than (~ 1.5 °C) the second intense event in 2006–2007 during 2002–2020 (Fig. 2a). The temporal evolution of the DMI during 2018–2019 showed strong temporal correspondence with the event during 2019–2020 and 2006–2007, such as the event developed during May–June, intensified during September–November, and terminated around December–January (Fig. 2a). However, the maximum magnitude of the DMI during the pIOD event in 2018–2019 was much smaller (~ 0.75 °C) than the events during 2019–2020 (~ 2.5 °C) and 2006–2007 (~ 1.5 °C) (Fig. 2a). The analysis of the SST anomalies in the western and eastern IOD zone during the peak phase of the pIOD events between October and November in 2006–2007 and 2019–2020 showed anomalous cooling in the eastern IOD zone and anomalous warming in the western IOD zone (Fig. 2b, c). These characteristics suggest that the higher values of the DMI during the peak phase of the events in 2006–2007 and 2019–2020 are determined by the combined effect of the cooling in the east and warming in the west (Fig. 2). However, between October and November in 2018–2019, the SST anomaly in the eastern IOD zone showed a near-climatological value, and the positive value of the DMI is primarily owing to the warming in the western IOD zone (Fig. 2).

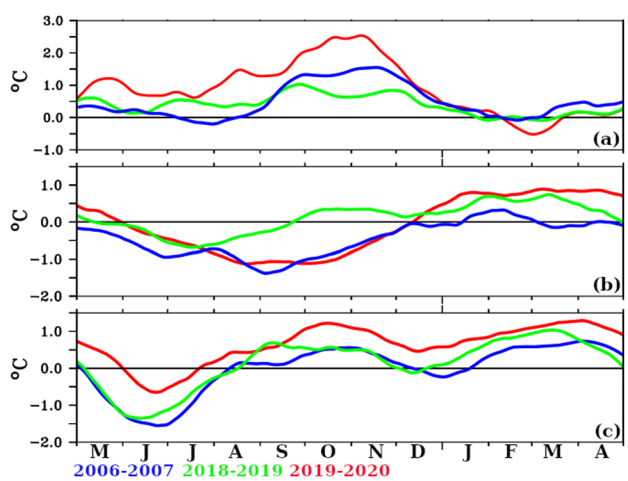

Fig. 2 Temporal evolution of the **a** DMI (°C) during 2006–2007 (blue), 2018–2019 (green), and 2019–2020 (red). Temporal evolution of the SST anomaly (°C) derived from the OI-SST in the **b** eastern IOD zone (10° S–Equator and 90° E–110° E) and **c** western IOD zone (50° E–70° E and 10° S–10° N) during 2006–2007 (blue), 2018–2019 (green), and 2019–2020 (red). A 30-day running mean is applied to all the parameters for better readability

The availability of the near-surface meteorological and sub-surface oceanographic parameters from the Research Moored Array for African-Asian-Australian Monsoon Analysis and Prediction (RAMA) buoy (McPhaden et al. 2009) at 5° S, 95° E in the eastern EIO provide an unprecedented opportunity to examine the underlying mechanisms that lead to the difference in the SSTA in the eastern EIO during the weak pIOD event in 2018–2019 and an extreme event in 2019–2020. The primary objective of the present study is to describe the nature of the SSTA in the eastern EIO associated with these two pIOD events and also to examine whether the factors that led to the cool SSTA in the eastern EIO during these two pIOD events play a similar role through the analyses of the mixed layer (ML) heat budget terms at 5° S, 95° E using the RAMA data.

Note that the RAMA mooring at 5° S, 95° E located is in the western periphery of the eastern IOD zone, where the cold SSTA associated with the pIOD event persists (Fig. 1c). As suggested by previous studies, the coastal ocean dynamics processes, such as the coastal Ekman pumping, along the coast of Sumatra and Java play an essential role in determining the SST variability in the eastern IOD zone's eastern margin (Horii et al. 2009; Delman et al. 2016, 2018). However, it is essential to note that the RAMA mooring at 5° S, 95° E is located in the western margin of the eastern IOD zone, where open ocean dynamics play an active role (Horii et al. 2009, 2013a, b). Understanding the underlying processes that determine the interannual SST variability in the open ocean region of the eastern EIO are equally crucial for a better

representation of the spatial spread of the SSTA associated with the pIOD events in the numerical model using seasonal, extended, and climate projections (Fig. 1c). The RAMA data was also available on relatively weak pIOD events in 2017–2018; however, this event was not considered for further analyses since the SSTA associated with this event at 5° S, 95° E was transient and nominal (Figure not shown).

Note that the previous studies have examined the ML heat budget in the eastern EIO during the pIOD events; however, these studies mainly depended on numerical model simulation and reanalysis products (Horii et al. 2009, 2013b; Santoso et al. 2010; Izuka et al. 2000; Vinayachandran et al. 2007; Delman et al. 2016; 2018; Wang et al. 2020). Using the ML heat budget analysis based on the Triangle Trans-Ocean Buoy Network (TRITON) data, Horii et al. (2009) examined the factors determining the cold SSTA associated with the pIOD event in 2006–2007 at 5° S, 95° E. Horii et al. (2009) also showed that, during the initial phase of the pIOD event in 2006–2007, the anomalous cooling was primarily determined by the net surface heat flux (*NHF*) loss from the ocean, while the horizontal advection determined the peak cooling phase between August and October.

In contrast to Horii et al. (2009), using ocean general circulation model output, Vinayachadran et al. (2007) demonstrated that the cooling due to the vertical processes also acted as an essential process along with the horizontal advection to determine the cold SSTA in the eastern EIO in association with the pIOD event in 2006 (Fig. 4a and 4b of Vinayachadran et al. 2007). Horii et al. (2009) attributed these discrepancies in the result to the difference in the study area compared to Vinayachandran et al. (2007), in which the latter one examined the ML heat balance in large areas which covered both open ocean and Sumatra and Java coasts, while in the former case the analysis was focused only at 5° S, 95° E. Note that the present study is an extension to the work carried out by Horii et al. (2009) using in-situ data at 5° S, 95° E during the pIOD event in 2006.

In the following discussion, we will examine the anomalous conditions that persisted at the RAMA mooring site at 5° S, 95° E during the pIOD events in 2019–2020 and 2018–2019. Subsequently, we will compare our result with Horii et al. (2009) to examine whether the factors that led to the cool SSTA in the eastern EIO (at 5° S, 95° E) in association with the pIOD event during 2006–2007 played a similar role during these two pIOD events.

The rest of the manuscript is organized as follows. Satellite and in-situ data used and methodology followed is summarized in Sect. 2. The results and discussion are presented in Sect. 3, and the results are summarized in Sect. 4.

2 Data and methods

2.1 Moored buoy data

For the analysis, near-surface meteorological and subsurface oceanographic measurements with one-day temporal resolution from the RAMA mooring at 5° S and 95° E were used (Fig. 1c). Subsurface measurements include water temperature at a depth of 1.5 m, 10 m, 20 m, 40 m, 60 m, 80 m, 100 m, 120 m, and 140 m, salinity at a depth of 1.5 m, 10 m, 20 m, 40 m, 60 m, 80 m, and 100 m and current velocity at a depth of 10 m. The buoy also measures near-surface atmospheric parameters such as the air temperature, relative humidity at a height of 3 m, wind velocity at a height of 4 m, and downwelling shortwave radiation at a height of 3.5 m above the sea surface. Note that RAMA salinity measurements at 1.5 m depth were not recorded from May 2018 to October 2019, and the measurements at 20 m and 80 m were also not available from May 2019 to October 2020. The subsurface temperature and salinity data were interpolated to 1 m to facilitate the analysis.

The latent (*LHF*) and sensible heat flux (*SHF*) are derived from COARE 3.0b bulk air-sea fluxes algorithm using the mooring SST, air temperature, and relative humidity (Fairall et al. 2003). Downwelling shortwave radiation obtained from RAMA mooring was corrected with a constant albedo (5.5%) to estimate the net shortwave radiation (*NSW*).

Downwelling longwave radiation (*DLW*) sensor was not equipped with RAMA mooring at 5° S and 95° E; hence, daily Clouds and the Earth's Radiant Energy System (CERES) *DLW* data with $1° \times 1°$ spatial resolution (Wielicki et al. 1996) was used to facilitate the analysis. We evaluated the quality of CERES *DLW* data with the measurements from RAMA mooring at 0° S and 80.5° E which is located approximately 1700 km away from the study region at 5° S and 95° E. The statistical analysis between the *DLW* at 5° S and 95° E showed a reasonably good agreement with a correlation of 0.8. Besides, the root mean square difference (RMSD) between these two *DLW* estimations was approximately 7.3 W m^{-2}, and this value was smaller than the standard deviations (~ 9.7 W m^{-2}) of long-time series of the RAMA *DLW* data at 0° S and 80.5° E. The above analysis implied that the CERES *DLW* data is a reliable replacement for the buoy data, and it can be used to estimate the net longwave radiation (*NLW*). The *NLW* at 5° S and 95° E were estimated after subtracting CERES *DLW* from black body radiation from the sea surface ($NLW = 0.97 \times (\sigma \times (\mathrm{SST} + 273.15)^4 - DLW)$; where σ is the Stefan–Boltzmann constant (5.67×10^{-8} W m^{-2} K^{-4}).

The daily climatology was estimated as the mean value for each day from the mooring data. However, there were

significant data gaps, and approximately 45% (~8.5 years) of data was only available for the meteorological parameters between 2002 and 2020 (Table 1). We evaluated the impact of the missing data on the climatology derived from the RAMA data with the estimation from the TropFlux data (2002–2018), which is generally considered as an excellent substitute for the in-situ near-surface meteorological and oceanographic parameters in the tropical Oceans (Praveen Kumar et al. 2012). It was found that the climatology of near-surface meteorological parameters derived from the RAMA mooring at 5° S and 95° E showed excellent agreement with the TropFLux climatology (Figs. S1 and S2). Similarly, climatology derived from CCMP wind speed data showed good correspondence with the measurements from the mooring (Fig. S1a). Hence, the analysis that follows is based on the climatology estimated from the mooring data. The daily anomaly fields were estimated by subtracting daily climatological values from the observed data.

The mixed layer depth (MLD) is defined as the depth where the density is equal to the sea surface density plus an increment equivalent to the density change (~0.125 kg m^{-3}) associated with a change in the temperature of 0.4 °C. The isothermal layer depth (ILD) is defined as the depth where the temperature is 0.4 °C lower than the SST. Barrier layer thickness (BLT) is defined as the difference between the ILD and MLD. Temperature inversions are defined to occur when the temperature at a depth is greater than the SST by 0.01 °C.

2.2 Satellite and Argo data

Daily National Oceanic and Atmospheric Administration (NOAA) Interpolated Outgoing Longwave Radiation (OLR) data (Liebmann and Smith 1996) at a spatial resolution of 2.5° were used as a proxy for convective activity in the EIO, and the positive (negative) value of the OLR anomaly represents suppressed (enhanced) convective activity. In addition, daily optimally interpolated (OI) SST products generated from the microwave (MW) and infrared (IR) SST data with a 9 km spatial resolution were used to explain the SST variability in the EIO (Gentemann et al. 2004). The daily average of the Cross-Calibrated Multi-Platform (CCMP) version 2 gridded surface vector winds (Atlas et al. 2011) with 0.25° spatial resolution and 6-h temporal resolution was used to describe the spatio-temporal evolution of the wind field in the EIO. A monthly average of the chlorophyll-*a* data from Moderate Resolution Imaging Spectroradiometer (MODIS) with a 4 km spatial resolution was used for the ML heat budget analysis. Gridded Argo salinity data generated through Variational Analysis (DIVA) interpolating method (Jha and Udaya Bhaskar 2020) was used to examine the salinity variability at the mooring location. Aviso daily gridded sea surface height anomaly (SSHA) with 0.33° resolution (AVISO Altimetry 2009) was used to describe the planetary wave activity at the EIO.

2.3 Mixed layer heat budget

The ML heat budget was evaluated using the equation given by Rao and Sivakumar (2000).

$$\rho C_p h \frac{\partial T}{\partial t} = NHF - \rho C_p h \left[u \frac{\partial T}{\partial x} + v \frac{\partial T}{\partial y}\right] + \rho C_p h H \left[W_h + \frac{\partial h}{\partial t}\right] \frac{(T_h - T)}{h} + \text{Residual} \quad (1)$$

(a) (b) (c) (d) (e)

Table 1 Percentage of the near-surface meteorological and oceanographic data available from the RAMA mooring at 5°S and 95° E during 2002–2020

Parameters	Percentage of data availability
Relative humidity (RH)	~59
Wind speed (WS)	~44
Air temperature (AT)	~63
SST	~93
Current speed	~47
NSW	~58
LHF	~44
SHF	~44
NLW	~93

The terms of the ML heat budget equation from left to right represent the (a) ML heat storage rate (b) the *NHF* is defined as the sum of the *NSW*, *NLW*, *LHF*, *SHF,* and Q_{PEN}, where the Q_{PEN} is the penetrative component of the shortwave radiation below the ML (c) horizontal advection (d) vertical processes and (e) residual. In Eq. 1, ρ is the density of the seawater (1025 kg m^{-3}), C_p is the specific heat capacity of the seawater (3903 J Kg^{-1} K^{-1}), h is the MLD in m, $\partial T/\partial t$ is the rate of change of the ML temperature in °C s^{-1}.

In equation one, $u\partial T/\partial x$ and $v\partial T/\partial y$ represent the zonal and meridional components of the horizontal advection term, respectively. The zonal (u) and meridional (v) current measurements at 10 m depth of the mooring were used to estimate the heat flux associated with the horizontal advection. The missing zonal and meridional current speed values between December 2018 and January 2019 were

linearly interpolated to facilitate the analysis. $\partial T/\partial x$ and $\partial T/\partial y$ are the zonal and meridional components of temperature gradient (°C m^{-1}), and they were estimated from the OI-SST daily gridded temperature data with a 9-km spatial resolution using a centred difference scheme. A two-point spatial box-car smoothing was applied to the satellite data before using a centred difference scheme to estimate the horizontal gradient. The heat flux associated with the horizontal advection may be sensitive to the choice of lateral smoothing prescribed on daily gridded SST data, and it is quantified as follows. The daily horizontal heat flux estimated from the gridded SST field before applying any box-car smoothing (defined as HF_BS; Δ(x,y) ~ 9 km) and after prescribing a four-point spatial smoothing (defined as HF_4S; Δ(x,y) ~ 36 km) compared with the estimation from our default choice (defined as HF_2S; Δ(x,y) ~ 18 km). Our analysis showed that the RMSD between HF_4S and HF_2S (HF_BS and HF_2S) was approximately 6.0 Wm^{-2} (4.5 W m^{-2}), and these differences were relatively small compared to the range of daily heat flux due to the horizontal advection (~ 55 W m^{-2}) observed in the study region. The above analysis indicated that the horizontal heat flux estimation did not change significantly with spatial smoothing of daily gridded SST data.

The vertical processes term consists of entrainment velocity at the base of the ML ($W_h + \frac{\partial h}{\partial t}$) and temperature gradient at the base of the ML ($\left(T_h - T\right)h^{-1}$). The entrainment velocity (in m day^{-1}) at the ML base was estimated from the rate of change of the MLD ($\partial h/\partial t$) and W_h. T_h is the temperature at 5 m below the MLD, which is entrained to the ML (Du et al. 2005).

Open ocean Ekman pumping due to the local wind stress curl, internal waves, and westward propagating Rossby waves play an important role in determining the W_h at the off-equatorial region, and their collective impact can be inferred from the upward and downward movement of the thermocline (Yu 2003; Girishkumar et al. 2013a). Following McPhaden (1982), vertical displacement of the isotherms in the thermocline was used to estimate the W_h. Past studies have demonstrated that the depth of the 23 °C isotherms (D23) can be used as a representative of the thermocline depth in the tropical Indian Ocean (Girishkumar et al. 2013a), and the W_h was estimated as the rate of change of the D23. H is the Heaviside step function [= 0 if ($W_h + \partial h/\partial t$) < 0, = 1 if ($W_h + \partial h/\partial t > 0$], which indicates that the vertical processes term is active only when the ML deepens relatively to the changes in the thermocline depth (McPhaden and Hayes 1991; Ashin et al. 2019).

We evaluated the heat flux due to the vertical processes sensitivity to the choice of isotherm to estimate the W_h. For that purpose, daily heat flux due to the vertical processes estimated using the rate of change of D23 was compared with the estimation based on the depth of 21 °C isotherm (VER_{Wh21}) and depth of 25 °C isotherm (VER_{Wh25}). The RMSD between VER_{wh21} (VER_{wh25}) and the estimation based on our default choice was around ~ 26 W m^{-2} (~ 33 W m^{-2}). Similarly, daily heat flux due to the vertical processes computed using the temperature at 1 m (VER_{Th1}), and 10 m (VER_{Th10}) below the MLD with our default choice (the temperature at 5 m below the ML) showed RMSD values of ~ 21 W m^{-2} and ~ 30 W m^{-2}, respectively. These differences were relatively small compared to the standard deviation (~ 44 W m^{-2}) of the daily heat flux associated with vertical processes estimated from the mooring data. The above analysis indicated that the heat flux estimation does not change significantly to the choice of isotherm to estimate the W_h and the depth below the MLD from water entrained into the ML.

The Q_{pen} was estimated using the expression proposed by Morel and Antoine (1994):

$$Q_{Pen} = 0.47NSW\left[V_1 e^{-h/\xi_1} + V_2 e^{-h/\xi 2}\right] \quad (2)$$

The value 0.47 represents the fraction of the *NSW* in the visible range (300–750 nm) incident on the sea surface, and the remaining 0.53 is the fraction of the infrared component (> 750 nm) of the *NSW* absorbed in the upper 2 m of the water column (Sweeney et al. 2005). ζ_1 and ζ_2 represent the e-folding lengths for the long visible and short visible wavelengths, h is MLD in meters, and V_1 and V_2 represent the percentage of the long visible and short visible wavelengths after removing the infrared component from the *NSW*. Values of ζ_1, ζ_2, V_1, and V_2 were estimated using MODIS monthly composite of chlorophyll-*a* (mg m^{-3}) data using the expression proposed by Morel and Antoine (1994). The monthly MODIS chlorophyll data were interpolated to a daily grid to estimate the daily values of the Q_{PEN}. The mean values of V_1, V_2, ζ_1, and ζ_2 at the mooring location were approximately 0.38, 0.62, 1.52 m, and 16 m.

The residual term consists of contributions from the unresolved processes such as the horizontal and vertical diffusivity, errors associated with a vertical resolution of sub-surface measurements, finite differencing computational errors, and the uncertainty in the parametrization of the penetrating shortwave radiations (Foltz and McPhaden 2009).

The influence of the absence of salinity observation on the accuracy of the MLD estimation from the buoy data was evaluated using relatively high vertical resolution measurements from an Argo float (WMO ID 2902149) located within 5° away from the mooring between 1 May 2018 and 1 January 2021 (Fig. 1; marked as pink dots in the bottom panel). The Argo float (WMO ID 2902149) measures temperature and salinity at every 5 m up to 50 m and every 10 m from 50 to 150 m. Note that the absence of salinity measurements at 80 m may not impact the MLD since the MLD was always shallower than 80 m during the study period. Argo data was sampled at RAMA buoy sensor depth

(defined as the Argo_R), and subsequently, we removed the values at 1.5 m, 40 m and 80 m from the Argo_R (defined as the Argo_R_M). The MLD estimation from Argo compared with the Argo_R and the Argo_RM to demonstrated the accuracy of the estimation from the mooring. The RMSD between Argo and the Argo_R (Argo_R and Argo_R_M) was around 6 m (4 m). These values were smaller than the variability in the MLD (standard deviation ~ 17 m) observed during the analysis period in the southeastern equatorial Indian ocean. The above results showed that the absence of salinity observations did not significantly impact the MLD estimation.

3 Results and discussion

3.1 Spatio-temporal evolution of the SST in the eastern EIO during the pIOD events in 2018–2019 and 2019–2020

Climatologically the SST evolution at the eastern EIO and mooring location exhibited an annual cycle with a maximum value (~ 30 °C) between April–May and a minimum value (~ 28.5 °C) around August–October with a progressively decreasing trend between May–August and increasing trend between November–April (Figs. 1a, 3a). It is worth pointing out that the temporal evolution of the SSTs at the mooring location during the two consecutive pIOD events that are of interest in the present study showed a similar annual cycle as apparent in the climatology (Fig. 3a).

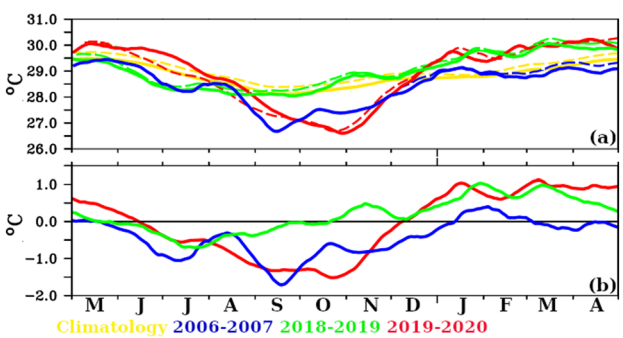

Fig. 3 Temporal evolution of the **a** SST (°C) and **b** SSTA (°C) from the OI-SST at RAMA mooring location at 5°S, 95°E in association with the pIOD events in 2006–2007 (blue), 2018–2019 (green), and 2019–2020 (red). The yellow line in panel (**a**) represents the SST climatology derived from satellite (°C; 2002–2020). The dashed lines in panel (**a**) represents MLT (°C; Climatology—yellow, 2018–2019—green, and 2019–2020—red) derived from RAMA mooring at 5° S, 95° E. Due to the absence of the sub-surface temperature and salinity measurements, the RAMA MLT was not represented for 2006–2007. A 30-day running mean is applied to all the parameters for better readability

The SSTA associated with the pIOD event during 2019–2020 was initiated as a faint zonal band of cold SSTA (~ − 0.3 °C) at the southern Java coast during May (Fig. 1c). This cold anomaly in the eastern EIO became more pronounced and intensified and spread south-westward during June–August (Fig. 1c). As the season progressed, the cold SSTA intensified further and reached its peak intensity by around October 2019 (~ > − 2 °C) and diffused by January 2020 (Figs. 1c, 3b). During its peak intensity during October 2019, the cold SSTA has shown the maximum westward spatial extent along the equator, and its signature is apparent up to 75°E (Fig. 1c). Subsequently, the SST in the eastern EIO had shown a warm anomaly from January 2020 onwards and reached its maximum value around April 2020 (~ 1 °C) (Figs. 1c). At the mooring location (5°S and 95°E), the SST remained warmer (~ 1 °C) than the climatological conditions until June in association with the event in 2019–2020 and subsequently showed cold SSTA during July–November with the peak value of ~ > − 1.5 °C around September–October (Fig. 3b). The maximum value of the warm SSTA at the mooring location during January–April in 2019–2020 reached as large as 1 °C (Fig. 3b). It is worth pointing out that the SSTA associated with the pIOD events during 2019–2020 and 2006–2007 had shown roughly similar characteristics at the mooring location (Fig. 3b). However, the SSTA between January and April in association with the event in 2006–2007 remained closer to the climatological conditions (Fig. 3b).

The SSTA in 2018–2019 showed a roughly similar spatio-temporal evolution compared to the event in 2019–2020, such as the cold SSTA initiated as small patches in the Java coast and intensified during July–August and did not show any further intensification during October–November and dissipated by December–January (Fig. 1b). In contrast to the event in 2019–2020, the magnitude of the cold SSTA in the eastern EIO in 2018–2019 was small (~ − 0.75 °C), and its spatial spread was restricted to a relatively smaller domain in the eastern EIO (Fig. 1b, c). At the mooring location, the magnitude of the cold SSTA was relatively weak (~ − 0.75 °C) and short-lived (June–September) during 2018–2019, compared to the event in 2019–2020 (Fig. 3b). During 2018–2019, the cold SSTA at the mooring location remained closer to the climatological conditions by the end of September 2018, approximately two months earlier than the event in 2019–2020 (Fig. 3a, b). However, the warm SSTA from January to March associated with the pIOD events in 2018–2019 and 2019–2020 had shown a comparable magnitude (Fig. 3b).

The causative mechanisms responsible for the difference in the SSTA between these two pIOD events are explained in the following sections.

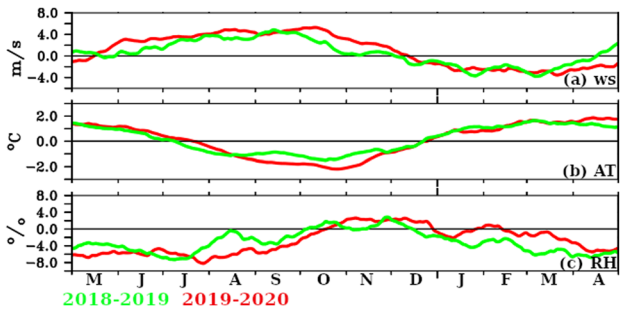

Fig. 4 Temporal evolution of the anomaly field of the **a** wind speed (m s^{-1}; *WS*), **b** air temperature (°C; *AT*) and **c** relative humidity (%; *RH*) obtained from the RAMA mooring at 5°S, 95°E in association with the pIOD events during 2018–2019 (green) and 2019–2020 (red). A 30-day running mean is applied to all the parameters for better readability. Please refer to Fig. S1 for the temporal evolution of the actual parameters

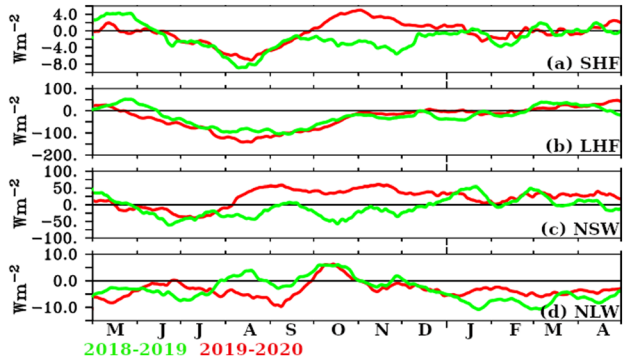

Fig. 5 Temporal evolution of the anomaly of the **a** sensible heat flux (*SHF*; W m^{-2}), **b** latent heat flux (*LHF*; W m^{-2}), **c** net shortwave radiation (*NSW*; W m^{-2}), and **d** net longwave radiation (*NLW*; W m^{-2}) derived from the RAMA mooring at 5° S, 95° E in association with the pIOD events during 2018–2019 (green) and 2019–2020 (red). Note that *DLW* data from CERES is used to estimate the *NLW*. A 30-day running mean is applied to all the parameters for better readability. A negative (positive) value of *SHF*, *LHF*, and *NLW* indicates enhancement (reduction) of heat loss from the ocean. Similarly, the negative (positive) value of *NSW* represents a reduction (enhancement) of heat gain by the ocean. Please refer to Fig. S2 for the temporal evolution of the actual parameters

3.2 The near-surface meteorological parameters at 5° S, 95° E

Climatologically wind speed exhibited a mild annual cycle with an increasing trend from May (< 4 ms^{-1}) onwards and reached its maximum magnitude (~ 4 ms^{-1}) around September–October and fell off (< 4 ms^{-1}) thereafter (Figs. 1a, 4a, S1a). The temporal evolution of the wind speed during 2019–2020 and 2018–2019 also showed an annual cycle as evident in the climatology (Fig. S1a). In association with the pIOD event in 2019–2020, the magnitude of the wind speed was anomalously high (~ 2 ms^{-1}) even in June, and subsequently, the anomalous wind speed conditions showed a progressively increasing trend and reached its maximum intensity (~ 4 ms^{-1}) around August (red line in Fig. 4a). From October 2019 onwards, the anomalous high wind speed conditions showed a decreasing trend and remained close to its climatological conditions from mid-December 2019 onwards (Figs. 4a, S1a).

Compared to 2019, the anomalous high wind speed conditions persisted only for a short duration from mid-July to mid-October in 2018–2019, though its magnitude from August to September had shown a comparable magnitude with respect to the event in 2019–2020 (green line in Fig. 4a). From December to May, the period followed by the pIOD event showed anomalous low wind speed conditions (~ − 2 ms^{-1}) during both these events (Fig. 4a).

The temporal evolution of the air temperature climatology also showed an annual cycle at the mooring location with a decreasing trend from July and reached its minimum value around October; subsequently, the air temperature showed an increasing tendency and reached peak value around December and did not show any significant variations in subsequent months (Fig. S1b). During the pIOD event in 2019, the air temperature was anomalously cold from August onwards and reached its maximum magnitude by the end of October (~ − 2.5 °C) (Fig. 4b). Subsequently, the cold anomaly associated with the air temperature showed a decreasing trend and became anomalously warm (~ 1.5 °C) from December 2019 to May 2020 (Fig. 4b). The temporal evolution of the air temperature anomaly in 2018–2019 showed a similar annual cycle as observed in 2019–2020, though the magnitude of the cold anomaly from August to November in the former case was slightly smaller (~ − 1 °C) compared to the latter case (Fig. 4b).

Relative humidity shows roughly similar temporal evolution during 2019–2020 and 2018–2019, with anomalous dry conditions (− 6%) during May–September, with maximum magnitude by the end of July, and remained close to its climatological conditions between October–January (Figs. 1c, 4c). The relative humidity anomaly field also showed an anomalous dry condition during February–April, though it was more prominent in 2018–2019 (Fig. 4c).

3.3 The radiative and turbulent heat fluxes at 5° S, 95° E

Climatologically, the heat loss from the ocean due to the *SHF* and *NLW* at the mooring locations showed an annual cycle with a mean value around − 8 W m^{-2} and − 50 W m^{-2}, respectively (Fig. S2a, S2d). However, the amplitude of the *SHF* (~ ± 4 W m^{-2}) and the *NLW* (~ ± 10 W m^{-2}) anomaly associated with the pIOD events are approximately a factor of 10 smaller compared to the anomalies of the *LHF*

(~ ± 150 W m^{-2}) and *NSW* (~ ± 75 W m^{-2}); hence, they are not discussed in the rest of the manuscript (Fig. 5a, d).

Climatological evolution of the *LHF* at the mooring location showed well defined annual cycle with a progressively increasing trend in the heat loss from the ocean from May to August and reached a maximum value by August (~ − 150 Wm^{-2}) (Fig. S2b; blue line). Subsequently, the *LHF* loss from the ocean showed a decreasing trend from August to November and reached a minimum value around November (~ − 100 W m^{-2}) and did not show any significant seasonal variability from November to April (Fig. S2b; blue line).

Temporal evolution of the *LHF* in 2018–2019 and 2019–2020 exhibited roughly similar annual cycles as observed in the climatology (Fig. S2b). In association with the pIOD event in 2019–2020, anomalous *LHF* loss from the ocean showed a progressively increasing and decreasing trend from May to October with a peak value around August (~ − 150 W m^{-2}) (Fig. 5b; red line). Subsequently, the *LHF* anomaly during 2019–2020 remained closer to the climatological conditions from November to February, and it showed a reduction in the heat loss from the ocean from March to April (~ 50 W m^{-2}) (Fig. 5b; red line). *LHF* anomaly during 2018–2019 also showed similar trends as observed during 2019–2020. The magnitude of reduction in the *LHF* loss from the ocean in 2018–2019 showed roughly similar magnitude as observed in 2019–2020 during November–April. However, the enhancement in the *LHF* loss from the ocean during May–September was relatively smaller in 2018–2019 (~ − 100 W m^{-2}) than the event in 2019–20 (~ − 150 W m^{-2}) (Fig. 5b).

The wind speed and air-sea-specific humidity difference are the primary factors that determine the *LHF* variability. The strong temporal correspondence between the *LHF* and the wind speed anomalies than the *LHF* and the sea-air specific humidity difference anomalies suggests that the anomalous wind speed plays an important role in determining the interannual *LHF* variability in the study region (Figs. 4a, 5b, 6). For example, the air-sea specific humidity difference anomaly showed a decreasing trend, while wind speed anomaly showed an increasing trend from May to August when *LHF* anomaly showed enchantment in the

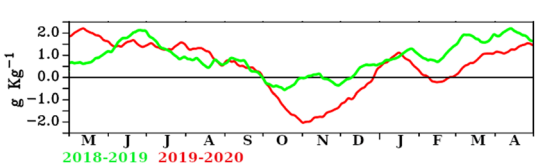

Fig. 6 Temporal evolution of the anomaly of the sea-air specific humidity difference ($q_s - q_a$; g kg^{-1}) derived from the RAMA mooring at 5° S, 95° E in association with the pIOD events during 2018–2019 (green) and 2019–2020 (red). A 30-day running mean is applied to the parameter for better readability. Please refer to Fig. S3 for the temporal evolution of the actual parameter

heat loss from the ocean in 2019–2020 (Figs. 4a, 5b, 6; red lines). In addition, a relatively higher correlation between the anomalies of the *LHF* and wind speed (~ 0.8) than the *LHF* and sea-air specific humidity difference (~ 0.12) during 2018–2020 further corroborated the dominant role of the wind speed on the *LHF* variability at the mooring location. These characteristics of the *LHF* anomaly apparent in 2019–2020 is consistent with the previous study by Horii et al. (2009), which showed that the enhancement in the wind speed is primarily responsible for the modulation of the *LHF* in the study region during 2006–2007. Besides, the temporal evolution of the *LHF* anomaly reported during the event in 2018–2019 and 2019–2020 is consistent with the event in 2006–2007 (Horii et al. 2009).

The climatology of the *NSW* also showed an annual cycle at 5° S, 95° E in the eastern EIO, with a minimum value (~ 175 W m^{-2}) around June–July and a maximum (~ 225 W m^{-2}) value around September–October (Fig. S2c; blue line). However, the *NSW* anomaly showed a reduction in the heat gain by the ocean from May to mid-August (~ − 25 W m^{-2}) and an enhancement in the heat gain by the ocean from mid-August to March (~ > 75 W m^{-2}) during the pIOD event in 2019–2020 (Fig. 5c; red line). Reduction in the convective activity in the eastern EIO is a typical signature of the pIOD event (Saji et al. 1999). Consistent with these features in the pIOD event, the spatio-temporal evolution of the OLR anomaly in the eastern EIO clearly showed a reduction in the convective activity (OLR anomaly > 40 W m^{-2}), the period when the *NSW* anomaly showed positive values during mid-August to March associated with the pIOD event in 2019–2020, suggests the strong relationship between these parameters (Fig. 7). The enhancement in the *NSW* due to the reduction in cloud cover in the eastern EIO in 2019–2020 was consistent with the event in 2006–2007 (Horii et al. 2009).

The magnitude of the positive OLR anomaly in the EIO was much smaller during 2018–2019 than in 2019–2020. Consistent with a weak positive OLR anomaly in the EIO, the *NSW* showed a mild reduction in heat gain by the ocean (~ > − 25 W m^{-2}) from June to January in 2018–2019 in contrast to the enhancement of the *NSW* in 2019–2020 (Fig. 5c). However, from February to April, the enhancement of the heat gain by the ocean showed comparable magnitude in 2018–2019 and 2019–2020. Moreover, the reduction in the heat gain by the ocean from June to August in 2018–2019 was consistent with the event in 2019–2020 (Fig. 5c).

Climatologically, the *NHF* showed an annual cycle with a heat loss from the ocean from May to October with a maximum heat loss around August (~ − 50 W m^{-2}) and heat gain by the ocean from November to April (~ 25 W m^{-2}). The *NHF* exhibited a well-defined annual cycle in 2019–2020 and 2018–2019; however, its temporal evolution differed from the climatology (Fig. 8b). The *NHF* showed anomalous

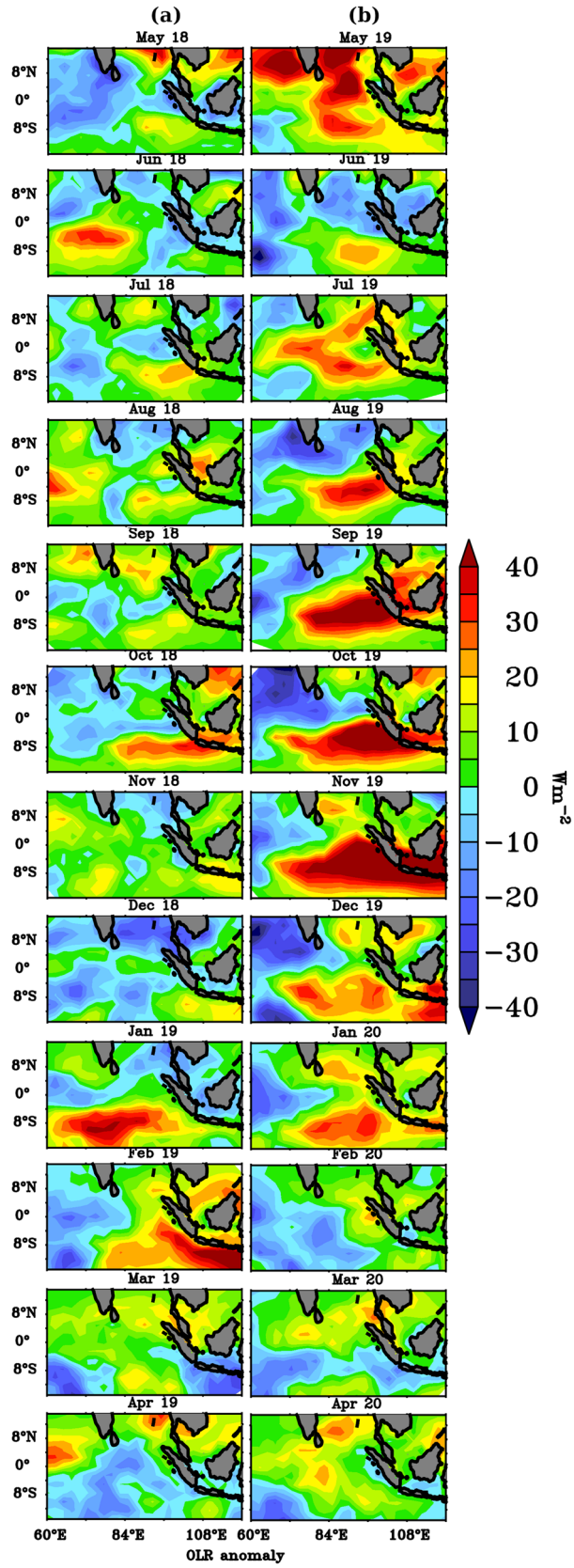

Fig. 7 Spatio-temporal evolution of the monthly average of the OLR anomaly (W m^{-2}) during the pIOD events in **a** 2018–2019, and **b** 2019–2020. The positive (negative) value of the OLR anomaly represents suppressed (enhanced) convective activity ▸

heat loss (~ − 150 W m^{-2}) from the ocean during the initial phase (May–July) of the pIOD event in 2019–2020 compared to its climatology (~ − 50 W m^{-2}) (Fig. 8b). Subsequently, *NHF* showed a reduction in heat loss from the ocean from August to September (~ − 25 W m^{-2}) than the climatology (~ − 50 W m^{-2}), and anomalous heat gain (~ 100 W m^{-2}) by the ocean than the climatology (~ 25 W m^{-2}) from October to December in 2019–2020 (Fig. 8b). The magnitude of the *NHF* in 2018–2019 and 2019–2020 showed comparable magnitudes during the initial phase of the pIOD event from May to July (Fig. 8b). However, in contrast to the event in 2019–2020, the anomalous heat loss from the ocean than the climatology was apparent from May to November in 2018–2019 (Fig. 8b). Between January–April, the *NHF* remained closer to its climatological conditions (~ 25 W m^{-2}) in 2019–2020; however, its magnitude showed heat gain and loss from the ocean on an intra-seasonal time scale in 2018–2019 (Fig. 8b).

3.4 Sub-surface hydrographic structure at 5° S, 95° E

Climatologically the near-surface hydrographic structure showed warm (28 °C) and low saline (34 psu) water over the cold (23 °C) and relatively high saline (35 psu) water (Figs. 9a, 10a). Furthermore, the seasonal evolution of the MLD showed an annual cycle with a deeper ML (~ 20 m) from June to October and shallow MLD (< 10 m) from March to May (Figs. 9a, 10a), and these characteristics were consistent with the seasonal cycle of the wind speed and *NHF* at the mooring location (Figs. S1a, 8b).

The presence of the halocline due to the existence of low saline water (34 psu) in the near-surface layer compared to the subsurface layer (35.2 psu) provided a conducive environment for the formation of the BL, and its thickness was relatively higher (~ 20 m) between June–November compared to other months (Figs. 9a, 10a). Though halocline is apparent during February–May, the BL was relatively thin (< 10 m) (Fig. 9a). These characteristics might be associated with the seasonality of the near-surface temperature structure, which showed relatively warm water in the near-surface layer during this period compared to the other months (Figs. 3a, 9a, 10a). Relatively large warming in the near-surface layer might have compensated the effect of halocline on the near-surface stratification, and this might be one of the plausible explanations of a thin BL during February–May (Figs. 9a, 10a).

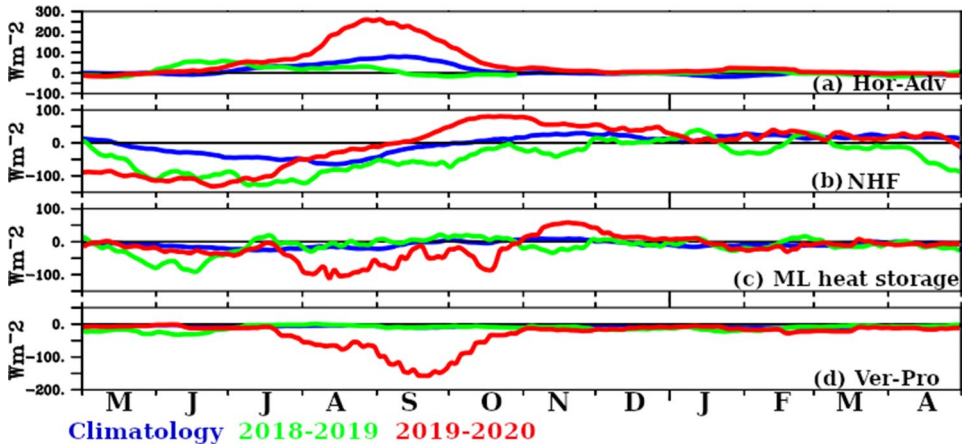

Fig. 8 Different terms in the ML heat budget equations derived from the RAMA mooring at 5° S, 95° E in association with the pIOD events during 2018–2019 (green) and 2019–2020 (red). The blue line represents the climatology (2002–2020) of the individual terms. **a** Horizontal advection, **b** *NHF*, **c** ML heat storage term, and **d** Vertical processes. Note that different vertical axes are used for each term. A 30-day running mean is applied to the parameters for better readability. Unit: W m^{-2}

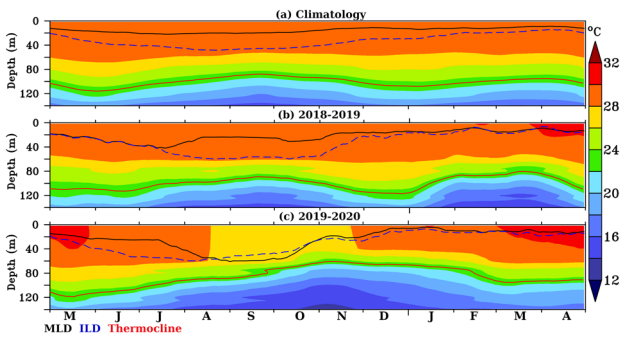

Fig. 9 Depth time section of the temperature (°C) derived from the RAMA mooring at 5° S, 95° E in association with the pIOD events in **a** climatology, **b** 2018–2019 and **c** 2019–2020. The thin red, thin black, and dashed blue lines represent the D23 (m), MLD (m), and ILD (m), respectively. A 30-day running mean is applied to the parameters for better readability. The difference between the MLD and ILD is defined as the BLT (m)

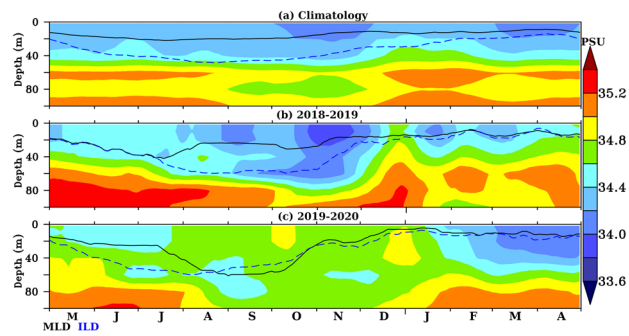

Fig. 10 Depth time section of the salinity (psu) derived from the RAMA mooring at 5° S, 95° E in association with the pIOD events in **a** climatology, **b** 2018–2019, and **c** 2019–2020. The thin black line and dashed blue lines represent the MLD (m), and the ILD (m), respectively. A 30-day running mean is applied to the parameters for better readability

The presence of the near-surface salt-stratification and thick BL can provide a conducive environment for the formation of inversion in the vertical temperature profile by trapping a significant part of the penetrating solar radiation below the shallow ML and relatively large cooling of the ML by the net surface heat loss and/or horizontal advection than the BL (Anderson et al. 1996; Kurian and Vinayachandran 2006; Girishkumar et al. 2013b). Climatologically, the formation of the TI depicted an annual cycle with a maximum frequency of occurrence (~30 to 40%) and strength (> 0.4 °C) between July to December, and subsequently, they showed a reduction in the frequency of occurrence (< 20%) and magnitude (< 0.2 °C) between January and June (Fig. 11a, d). Most importantly, the formation of the TI showed strong temporal correspondences with the BLT, such as the occurrence of the relatively strong TI was relatively more frequent during June–November compared to the other months (Fig. 11a, d).

As a result of the near-climatological state of the thick BL and shallow ML, the seasonality of the formation of the TI between June 2018 and May 2019 at the mooring location showed roughly similar characteristics as depicted in the climatology (Figs. 9, 10, 11). Such as approximately 30–60% of profiles showed the occurrence of moderately strong temperature inversion (~0.2 °C) during August–December

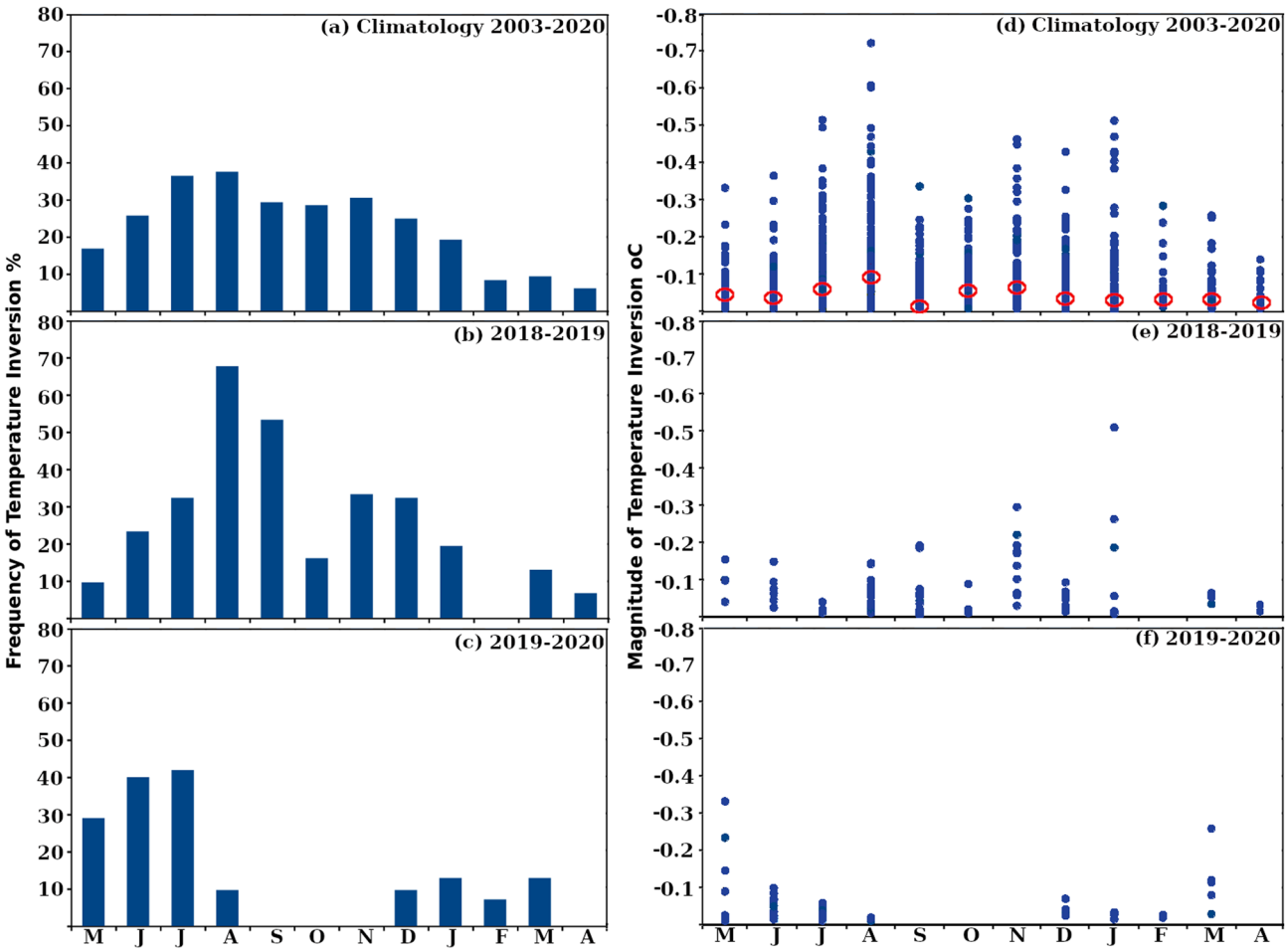

Fig. 11 Monthly evolution of (right panels) frequency (%) of occurrence of the temperature inversion (TI) of magnitude greater than 0.01 °C and (left panels) magnitude of TI (°C) derived from the RAMA mooring at 5° S, 95° E. **a**, **d** Climatology, **b**, **f** 2018–2019 and **c**, **g** 2019–2020. In panel **d**, the red open circles represent the monthly mean value of the TI magnitude (°C)

2018 compared to the relatively few cases of the TI (< 10%) between January and May 2019 (Figs. 8a, b, 9a, b, 11b, e).

However, the MLD was relatively deeper (~ 60 m) during June–December 2019, due to absence of the near-surface halocline and higher wind speed in contrast to the climatological conditions at the mooring location (Figs. 4a, 9c, 10c). Note that the absence of the halocline in 2019–2020 was also apparent in the gridded Argo salinity data at the mooring location (Fig. S4b). Consistent with the deeper MLD and the absence of halocline, BL was roughly absent during August–December in 2019–2020 compared to 2018–2019 and climatology (Figs. 9, 10). As a result of an unfavourable environment for the TI formation, such as the thin BL and absence of near-surface salinity stratification, TI was absent during September–November, 2019 (Fig. 11c, f).

The seasonality of the D23 (a proxy for the thermocline depth) showed a strong semi-annual cycle with a relatively shallow (~ 70 m) thermocline during August–October and March–April and a slightly deeper (~ 120 m) thermocline in between these two periods (Fig. 9a). These characteristics in the seasonality in the thermocline depths were consistent with the semi-annual planetary wave dynamics in the EIO (Yu et al., 1991; Yu 2003; Rao et al., 2010). The temporal evolution of the D23 showed roughly similar characteristics as apparent in the climatological state during 2018–2019. However, the D23 depicted an annual cycle in 2019–2020 compared to the semi-annual cycle in 2018–2019, primarily due to the absence of the deepening phase of thermocline during October–December (Fig. 9). In contrast to the climatology and 2018–2019, the D23 showed a progressively shallowing tendency from June to December (Fig. 9c). Note that during October–November in 2019–2020, the D23 reached as shallow as ~ 60 m, in contrast to ~ 120 m in 2018–2019 (Fig. 9).

As reported by the past studies, the anomalous shallow thermocline at the mooring location during October–November in 2019 was a typical signature of the pIOD events due to an anomalous westward propagating upwelling

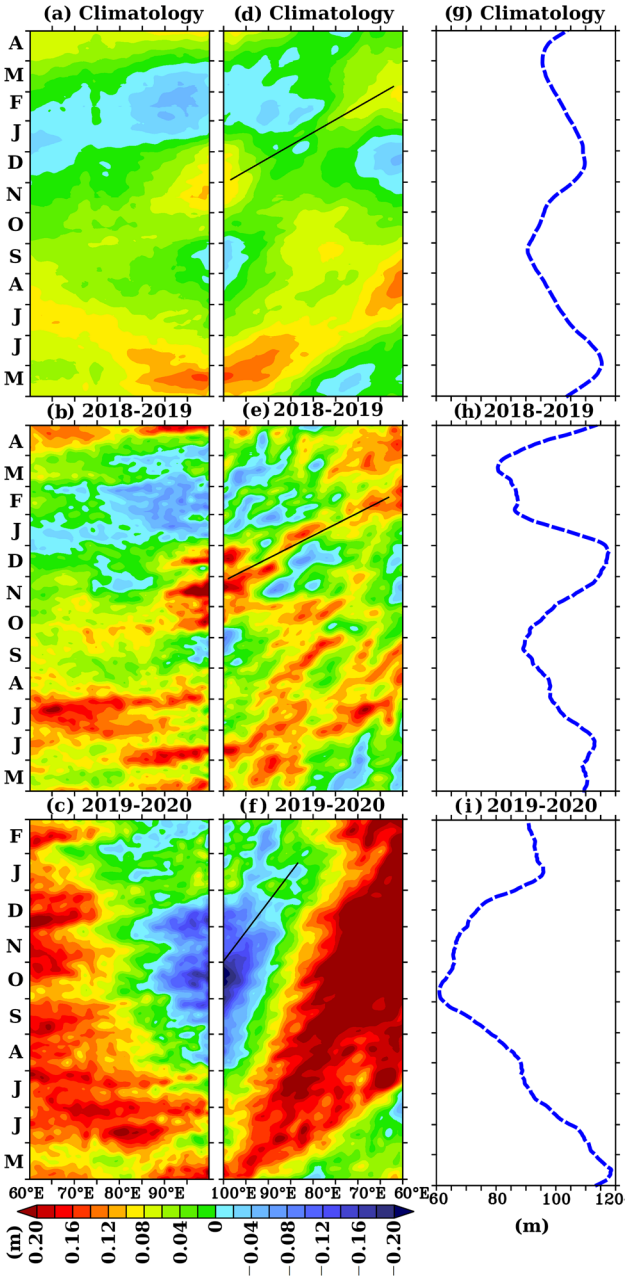

Fig. 12 Hovmöller diagram of the SSHA (m) **a**–**c** along the equator (averaged over 1° N–1° S), **d**–**f** along 5°S (averaged over 4° S–6 °S; note the east–west reversal in the x-axis), and **g**–**i** D23 (m) derived from RAMA mooring at 5° S, 95° E. (top panels; **a**, **d** and **g**) Climatology (2002–2020), (middle panels; **b**, **e**, and **h**) during 2018–2019, and (bottom panels; **c**, **f** and **i**) 2019–2020. The thin black line in panels in the second column represents the upwelling Rossby waves in 2019–2020 instead of the downwelling Rossby waves as in (middle panels) 2018–2019 and (top panels) the climatology from September to December at the mooring location at 5° S, 95° E. Note that data only up to February 2020 is presented in the bottom panel due to the non-availability of the data

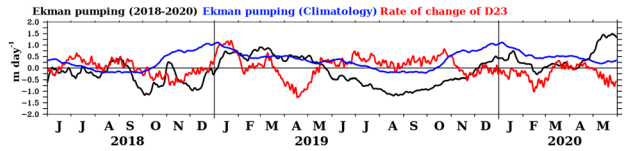

Fig. 13 Temporal evolution of the Ekman pumping velocity (m day^{-1}) during 2018–2019 (black), and its climatology (2002–2020; blue) and rate of change of D23 (red). A 30-day running mean is applied to the parameter for better readability

Rossby wave (Potemra et al. 1997; Murtugudde et al. 2000; Schott et al. 2009). As demonstrated by the past studies, the anomalous easterly wind anomaly in the EIO during October–November led to the generation of anomalous upwelling Kelvin waves in the eastern EIO, and when these waves traversed as coastal Kelvin waves along the Sumatra and Java coast, which then radiated westward as the low baroclinic mode upwelling Rossby waves into the interior (Potemra et al. 1997; Murtugudde et al. 2000; Schott et al. 2009) (Fig. 12c, f, i). The signature of the upwelling Kelvin waves in the eastern EIO and upwelling Rossby waves along 5° S in response to the anomalous easterly wind in the EIO was apparent as the negative value in SSHA (Figs. 1c, 12c, f, i). In contrast to the event in 2019–2020, as a consequence of a near climatological state in October–November, such as the downwelling Kelvin waves in the EIO and westward propagating downwelling Rossby waves along 5° S, the thermocline was deeper at the mooring location in 2018–2019 (Figs. 1a, b, 12a, b, d, e, g, h).

In addition to the westward propagating Rossby waves, local upwelling (downwelling) associated with divergence (convergence) of the Ekman currents associated with the cyclonic (anticyclonic) wind stress curl can also modulate the thermocline variability (Yu 2003).

Following Yu (2003), Ekman pumping velocity (EPV) at the base of the Ekman layer can be expressed as follows

$$EPV = \frac{1}{\rho_0}\left(\left(\nabla \times \tau_0\right) + \frac{\beta \tau_0^x}{f}\right) \tag{3}$$

where $\tau_0 = \left(\tau_0^x, \tau_0^y\right)$ is the surface wind stress derived from CCMP wind velocity data, ρ_0 is the mean density of the seawater, β is the meridional gradient of the Coriolis parameter f.

Climatologically EPV showed a mild downwelling tendency (~ − 0.25 m day^{-1}) between July and October and an upwelling tendency between November and May with a peak value around the end of the calendar year (1 m day^{-1}) (Fig. 13). However, during October–November, 2019, when the thermocline depth was anomalously shallow, the local EPV showed a strong downwelling tendency (> − 1 m day^{-1}) (Fig. 13). This characteristic suggested that the anomalous

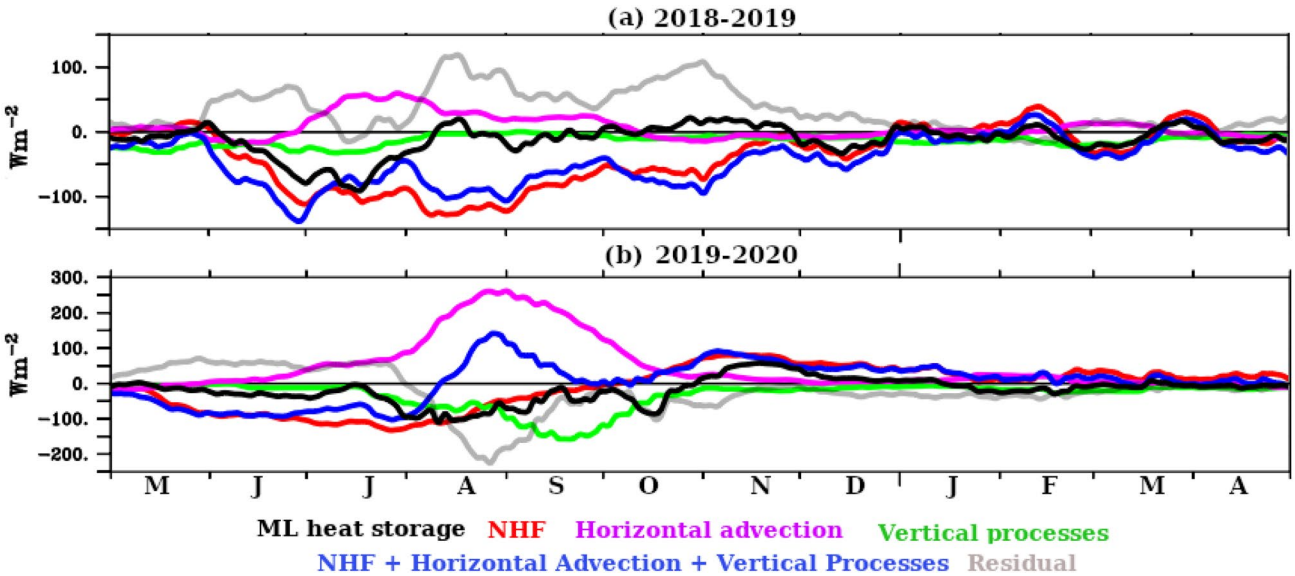

Fig. 14 Different terms in the ML heat budget equations derived from the RAMA mooring at 5° S, 95° E in association with the pIOD events during **a** 2018–2019 and **b** 2019–2020. The ML heat storage rate (black), *NHF* (red), horizontal advection (pink), vertical processes (green), the sum of the *NHF*, horizontal advection, vertical processes (blue), and residual (grey). Note that different vertical axes are used for the years **a** 2018–2019 and **b** 2019–2020. A 30-day running mean is applied to all the parameters for better readability. Please refer to Fig. 8 to compare each term with respect to its climatology. Units: W m^{-2}

Table 2 The mean value of vertical temperature gradient ($(T_h - T)\times h^{-1}$;$\times 10^{-3}$ ℃ m^{-1}) and entrainment velocity ($H(W_h + \frac{\partial h}{\partial t})$; m day^{-1}) at the base of ML during August–November, in climatology, 2018 and 2019

Parameters	Climatology	2018	2019
$H(W_h + \frac{\partial h}{\partial t})$ (m day^{-1})	2.04 ± 0.1	3.10 ± 0.6	1.14 ± 0.2
$(T_h - T)\times h^{-1}$ ($\times 10^{-3}$ ℃ m^{-1})	− 5.37 ± 0.1	− 7.65 ± 0.9	− 28.49 ± 0.6

shallow thermocline at the mooring location during October–November 2019 was primarily due to the westward propagating anomalous upwelling Rossby wave.

3.5 Mixed layer heat budget analysis at 5° S, 95° E

We will start with the ML heat budget during 2019–2020. The ML heat storage tendency generally showed reasonably good agreement with the sum of the *NHF*, horizontal advection, and vertical processes (Fig. 14b). During the initial cooling phase from May to July in 2019–2020, *NHF* acted as the dominant factor (~ − 125 W m^{-2}) to modulate the ML heat storage term (~ − 25 to − 50 W m^{-2}). The contribution of the vertical processes was negligibly small (~ − 50 W m^{-2}), and the warming tendency associated with the horizontal advection processes (~ 50 W m^{-2}) dampened the cooling tendency associated with the *NHF* from May to July in 2019–2020 (Figs. 8b, 14b).

Between August and October 2019, when the ML heat storage rate showed a substantial cooling tendency (~ < − 100 W m^{-2}), the role of the *NHF* on the ML cooling was significantly reduced from ~ > − 100 to ~ − 50 W m^{-2} between August and September, and it showed heat gain by the ocean in October (Figs. 8b, 14b). In contrast to the *NHF,* the vertical processes term (~ − 175 W m^{-2}) acted as the predominant factor in determining the ML colling tendency from August to October in 2019–2020 (Figs. 8b, 14b).

Note that the warming tendency associated with the horizontal advection processes (~ 250 W m^{-2}) reached its maximum magnitude during August–October and tried to dampen the combined effect of the cooling tendency associated with the *NHF* and vertical processes in 2019–2020 (Figs. 8a, b, 14b).

In general, the cooling tendency associated with the vertical processes term remained close to its climatological condition (~ − 10 W m^{-2}) in 2018–2019 (Fig. 8d). However, during May–June, the contribution of the vertical processes term (~ − 25 W m^{-2}) in 2018–2019 was higher than 2019–2020 and the climatology (Fig. 8d). The cooling tendency associated with the vertical processes' terms showed a much smaller magnitude (~ − 10 W m^{-2}) during August–October in 2018–2019, when this term showed an anomalous heat loss from the ML in 2019–2020 (Fig. 8d). The existence of the anomalous hydrographic conditions such as the relatively shallow thermocline, weak near-surface salinity stratification, thin BL, and an absence of the temperature inversion in conjunction with an anomalous

deepening of the ML due to anomalous higher wind speed provided a conducive environment for much freer turbulent exchange of the sub-surface cold water to the near-surface layer from August to October in 2019–2020 (Figs. 8d, 9, 10, 11). On the other hand, the near-climatological states of the thick BL and deeper thermocline led to a relatively small cooling tendency due to the vertical processes in 2018–2019 (Figs. 8d, 9, 10, 11).

The relative contribution of the entrainment velocity and temperature gradient at the base of the ML on the anomalous cooling due to the vertical heat flux during the peak cooling phase associated with the pIOD event between August and November is evaluated (Table 2). The entrainment velocity was a factor of two smaller in 2019 (1.14 m day^{-1}) compared to its climatology (2.04 m day^{-1}) and 2018 (3.10 m day^{-1}). Conversely, the temperature gradient at the base of the ML in 2019 (-28.49×10^{-3} °C m^{-1}) was a factor of four higher than 2018 (-7.65×10^{-3} °C m^{-1}) and a factor of five higher than its climatology (-5.37×10^{-3} °C m^{-1}) (Table 2). The above analysis depicted that the anomalous cooling due to the vertical processes during the peak cooling phase in 2019 was primarily owing to the anomalous temperature gradient at the base of the ML. A large temperature gradient at the bottom of the ML in 2019 was mainly due to the relatively thin BL. In the case of the thin BL, as observed in 2019, the base of the ML was nearly identical to the top of the thermocline, and it led to the relatively large negative value of the temperature gradient at the bottom of ML (Girishkumar et al. 2017). When the BLT was strong, as observed in the climatology and 2018 at the study region during August-November, the temperature at the base of the ML was either nearly identical to the MLT or higher than the MLT due to the existence of temperature inversion. This situation led to the relatively small negative (positive) values of the temperature gradient at the base of the ML in the case of the thick BL without TI (with TI) (Girishkumar et al. 2017).

The warming tendency due to the horizontal advection from June to October was also apparent in 2018–2019 and climatology (~75 W m^{-2}), though its magnitude was much lesser than the event in 2019–2020 (~250 W m^{-2}) (Fig. 8a). Based on the numerical model output, previous studies have also reported that the warming tendency was due to the horizontal advection in the coastal ocean region of the eastern EIO from June to October (Figs. 15b and 15d of Du et al. 2005). These characteristics also suggested that the anomalous warming tendency due to the horizontal advection at the mooring location during August-October in 2019–2020 was a manifestation of the enhancement of the seasonal cycle (Fig. 8a). It is worth pointing out that the warming tendency due to the horizontal advection process during the cooling phase of the SST from August to October in 2019–2020 and 2018–2019 contradicted with the study by Horii et al. (2009). They showed that the cooling tendency associated with the horizontal advection process played a vital role in determining the anomalous cool SST in a relatively strong pIOD event in 2006 at the same mooring location.

During October–April in 2019–2020, the period followed by the intense cooling, the warming tendency in the ML heat storage rate (~50 W m^{-2}) was primarily modulated by the *NHF* (~50 W m^{-2}) and secondarily by the horizontal advection processes (~25 W m^{-2}), while the vertical processes term (~−25 W m^{-2}) tried to cool the ML (Figs. 8, 14b). Roughly similar characteristics were observed from October to April in 2018–2019. The primary role played by the *NHF* on the warming phase of the SST after the peak cooling phase in October due to reduction in the *LHF* loss from the ocean and enhancement in the *NSW* heat gain by the ocean, was consistent with Horii et al. (2009)

3.6 Decomposition of the horizontal advection processes terms

The above analysis showed that the warming due to the horizontal advection process during the peak cooling phase of the SST in 2019–2020 contradicted the study by Horii et al. (2009). To quantify the relative contributions of the anomalous surface currents and lateral SST gradients on the anomalous warming due to the horizontal advection term during the peak cooling phase associated with the pIOD event between August and November 2019, the zonal and meridional heat advection terms decomposed into climatology and its anomaly as follows (Horii et al. 2009),

$$-U\frac{\partial T}{\partial x} = -\langle U\rangle\langle\frac{\partial T}{\partial x}\rangle - \langle U\rangle\frac{\partial T}{\partial x}' - U'\langle\frac{\partial T}{\partial x}\rangle - U'\frac{\partial T}{\partial x}' \quad (4)$$

$$-V\frac{\partial T}{\partial y} = -\langle V\rangle\langle\frac{\partial T}{\partial y}\rangle - \langle V\rangle\frac{\partial T}{\partial y}' - V'\langle\frac{\partial T}{\partial y}\rangle - V'\frac{\partial T}{\partial y}' \quad (5)$$

Table 3 The decomposition of zonal and meridional heat fluxes ($\times10^{-2}$ °C day^{-1}) into the individual terms on the right-hand side of expressions (4) and (5)

Zonal ($\times10^{-2}$ °C Day^{-1})	$-U\frac{\partial T}{\partial x}$	$-\langle U\rangle\langle\frac{\partial T}{\partial x}\rangle$	$-\langle U\rangle\frac{\partial T}{\partial x}'$	$-U'\langle\frac{\partial T}{\partial x}\rangle$	$-U'\frac{\partial T}{\partial x}'$
Average	0.54 ± 0.10	0.04 ± 0.02	-0.29 ± 0.01	0.02 ± 0.004	0.76 ± 0.11
Meridional ($\times10^{-2}$ °C Day^{-1})	$-V\frac{\partial T}{\partial y}$	$-\langle V\rangle\langle\frac{\partial T}{\partial y}\rangle$	$-\langle V\rangle\frac{\partial T}{\partial y}'$	$-V'\langle\frac{\partial T}{\partial y}\rangle$	$-V'\frac{\partial T}{\partial y}'$
Average	4.03 ± 0.36	1.41 ± 0.17	0.62 ± 0.18	2.25 ± 0.23	-0.28 ± 0.22

In expressions (4) and (5) the climatologies are enclosed in angle brackets and anomalies denoted by the prime symbol. The terms $(-\langle U\rangle\langle\frac{\partial T}{\partial x}\rangle, -\langle V\rangle\langle\frac{\partial T}{\partial y}\rangle)$ represents the climatological heat advection, $(-U'\frac{\partial T}{\partial x}', -V'\frac{\partial T}{\partial y}')$ represents the contribution due to anomalous horizontal current speed and anomalous lateral SST gradient, $(-\langle U\rangle\frac{\partial T}{\partial x}', -\langle V\rangle\frac{\partial T}{\partial y}')$ represents contribution due to climatological horizontal current speed and anomalous temperature gradient, and $(-U'\langle\frac{\partial T}{\partial x}\rangle$, $-V'\langle\frac{\partial T}{\partial y}\rangle)$ represents contribution due to anomalous horizontal current and climatological SST gradient and the average values of these terms between August and November 2019 presented in Table 3.

Our analysis showed that the meridional heat flux $(-\langle V\rangle\langle\frac{\partial T}{\partial y}\rangle; 1.41\times10^{-2}$ °C day$^{-1})$ acted as a predominant term than the zonal $(-\langle U\rangle\langle\frac{\partial T}{\partial x}\rangle; 4.30\times10^{-4}$ °C day$^{-1})$ in determining the warming due to the horizontal advection in climatology during August–November (Table 3). As observed in the climatology, heat flux due to the meridional advection $(-V\frac{\partial T}{\partial y}; 4.03\times10^{-2}$ °C day$^{-1})$ was approximately a factor of seven higher than the zonal advection $(-U\frac{\partial T}{\partial x}; 5.4\times10^{-3}$ °C day$^{-1})$ during August–November, 2019 (Table 3). This characteristic further supported our argument that the anomalous warming by horizontal advection processes as observed during the peak cooling phase of the SST between August–November in 2019 was an enhancement of the seasonal cycle (Fig. 8a). Besides, the decomposition of the horizontal heat flux term depicted that the anomalous zonal heat flux during August–November 2019 was primarily determined by the $-U'\frac{\partial T}{\partial x}'$, $(7.6\times10^{-3}$ °C day$^{-1})$, while the cooling tendency associated with the $-\langle U\rangle\frac{\partial T}{\partial x}'$ $(-2.9\times10^{-3}$ °C day$^{-1})$ dampened the warming tendency associated with other terms (Table 3). In contrast, the anomalous meridional heat flux during August–November 2019 was primarily determined by $-V'\langle\frac{\partial T}{\partial y}\rangle$ $(2.25\times10^{-2}$ °C day$^{-1})$. The above analysis suggested that the anomalous southward current and the climatological meridional temperature gradient predominantly determined the anomalous warming from August to November 2019. This aspect is depicted in Fig. S5, such as the zonal current during August-November, 2019 showed weak eastward flow (0.02 ms^{-1}) compared to the westward current (-0.08 m s^{-1}) in climatology and 2018. However, the magnitude of the meridional current showed strong southward flow (-0.25 m s^{-1}) during August–November 2019, compared to its climatology and 2018 (~-0.08 m s^{-1}) (Fig. S5). This result contradicted with Horii et al. (2009), which showed that the anomalous cooling due to the horizontal advection from August to November 2006 was primarily determined by the $-U'\frac{\partial T}{\partial x}'$ and secondarily by $-V'\langle\frac{\partial T}{\partial y}\rangle$.

4 Summary and conclusion

The Indian Ocean Dipole (IOD) event, one of the dominant interannual coupled ocean–atmosphere phenomena in the tropical region, plays an important role in modulating the climatic conditions in the Indian Ocean and different parts of the globe. The analysis of the DMI data during the last 19 years (2002–2020) showed that the Indian Ocean hosted two pIOD events with an extremely strong pIOD event in 2019–2020 and a relatively weak event in 2018–2019. The DMI magnitude associated with the event in 2019 reached as large as 2.5 °C, which was approximately a factor of two higher than (~ 1.5 °C) the second intense event in 2006–2007. However, the maximum magnitude of the DMI between September–November during the pIOD event in 2018–2019 was much smaller (~ 1 °C) than the event during 2019–2020.

In response to these two pIOD events, the SSTA in the western periphery of the eastern IOD zone at 5° S, 95° E showed distinct temporal evolution. Such as, in response to the event in 2019–2020, SST at the mooring location was anomalously cold during August–December with a peak value of − 1.5 °C around October, and subsequently anomalous warm water (1 °C) was apparent during January–April. The magnitude of the cold SSTA was relatively weak (− 0.75 °C) and short-lived (June–September) during 2018–2019, compared to the event in 2019–2020. However, the magnitude of warm SSTA showed a comparable magnitude between December–April in 2018–2019 and 2019–2020.

In association with the two pIOD events, the wind speed was anomalously high (low) with a progressively increasing and decreasing trend from June to November (January to April) with a maximum (minimum) value around August (March). Besides, the anomalous low wind speed conditions from January to April, followed by the pIOD events, showed comparable magnitude between the events (~ 2 m s^{-1}) in 2019–2020 and 2018–2019. However, from June to November, anomalous high wind speed (~ 4 m s^{-1}) was relatively more persistent in 2019–2020 than in 2018–2019.

The *LHF* showed an anomalous enhancement (reduction) in the heat loss from the ocean from May to October (November to April) with a magnitude of ~ − 150 W m^{-2}(~ 50 W m^{-2}) during 2018–2019 and 2019–2020. However, the anomalous *LHF* loss from May to October was more pronounced in 2019–2020 than in 2018–2019. It was also found that the anomalous conditions in the wind speed was primarily determined the *LHF* anomaly during the pIOD events.

With respect to the anomalous reduction in the convective activity in the EIO, the *NSW* showed anomalous heat gain by the ocean from August to March (~ 100 W m^{-2}) in

2019–2020. However, the reduction in convective activity in 2018–2019 was not pronounced as evident in 2019–2020; consequently, the *NSW* showed the reduction in heat gain by the ocean from September to January in 2018–2019 compared to the enhancement in 2019–2020.

Our ML heat budget analysis suggested that the enhanced cooling due to the vertical processes and *NHF* determined the anomalous cooling during June-October in association with the pIOD event in 2019–2020. The combined effect of an anomalous thin barrier layer, shallow thermocline, weaker near-surface haline stratification, and strong wind-induced vertical mixing led to the cooling due to the vertical processes, while the enhanced *LHF* loss from the ocean increased the *NHF* loss from the ocean.

Our analysis also suggested that the absence of a dominant cooling tendency associated with the vertical processes as apparent in 2019–2020 must be the primary reason for the relatively small cooling during August–October in 2018–2019. Relatively thick BL, deeper thermocline, strong near-surface haline stratification, and weak wind speed similar to the climatological conditions in 2018–2019 inhibited the vertical transfer of cold thermocline water to the near-surface layer compared to the event in 2019–2020. Instead of the vertical processes, an anomalous *LHF* loss from the ocean and reduction in the *NSW* acted as the critical processes to determine the cooling tendency during the initial phase of the pIOD event in 2018–2019, in which the latter parameter counteracted the cooling tendency in 2019–2020.

Our analysis indicated that the warming tendency associated with the horizontal advection processes dampened the cooling tendency associated with the vertical processes and *NHF* from August to October during the pIOD events in 2018–2019 and 2019–2020. The warming tendency due to the horizontal advection process during the cooling phase of the SST from August to October in 2019–2020 contradicted the study by Horii et al. (2009). They showed that the cooling tendency associated with the horizontal advection process played an essential role in determining the anomalous cool SST in a relatively strong pIOD event in 2006 at the mooring location.

In summary, our result suggested a year-to-year deviation in the factors that led to the cool SSTA at the western periphery of the eastern IOD zone. Note that the contribution of the residual showed a comparable magnitude with other terms in the ML heat budget. These characteristics suggested that in addition to the error associated with the calculation of various terms in the ML heat budget, the processes such as the diapycnal heat flux at the base of the ML (Moum et al. 2013) may also played an important role to determine the SST anomaly associated with pIOD event in the southeastern equatorial Indian Ocean. The incorporation of microstructure sensors in the selected depth in the mooring at 5°S, 95°E, similar to Moum et al. (2013), may provide valuable insight in that direction.

Our analysis also indicated that it is necessary to accurately represent the three-dimensional process in the ocean model to simulate the spatial–temporal evolution of the SST anomalies associated with pIOD events in the eastern EIO. Hence, it is imperative to evaluate the skill of gridded reanalysis products (Carton et al. 2018; Forget et al. 2015; Ravichandran et al. 2013) to replicate the conclusions drawn from the mooring data during the pIOD events. This topic is beyond the scope of the present work, and it will be addressed as a separate study. Besides, the plausible mechanism that leads to consecutive pIOD events in 2018–2019 and 2019–2020 is also a topic for future research.

Supplementary Information The online version contains supplementary material available at https://doi.org/10.1007/s00382-021-06099-8.

Acknowledgements The encouragement provided by the Director, INCOIS is gratefully acknowledged. The authors thank two anonymous reviewers and Dr. Takanori Horii, Japan Agency for Marine-Earth Science and Technology (JAMSTEC) for their extensive and constructive comments and suggestions which greatly helped to improve the manuscript. Ms. Aparna has carried out this work as part of her masters dissertation work. RAMA data quality controlled and distributed by Global Tropical Moored Buoy Array (GTMBA) project office of NOAA/Pacific Marine Environmental Laboratory, RAMA data are available from PMEL (https://www.pmel.noaa.gov/gtmba/pmel-theme/indian-ocean-rama). Microwave-Infrared OI SST data are produced by Remote Sensing Systems and sponsored by National Oceanographic Partnership Program (NOPP) and the NASA Earth Science Physical Oceanography Program. Data are available at www.remss.com. MODIS Aqua chlorophyll data is distributed by NOAA-CoastWatch, and data is available at https://oceanwatch.pfeg.noaa.gov/thredds/Satellite/MH1/chla/catalog.html?dataset=satellite/MH1/chla/8day. CCMP Version-2.0 vector wind analyses are produced by Remote Sensing Systems. Data are available at www.remss.com. The DMI data used in the study is made available by NOAA/ESRL, and data is available at https://stateoftheocean.osmc.noaa.gov/sur/ind/dmi.php. The altimeter products were produced by Ssalto/Duacs and distributed by Aviso+, with support from Cnes (https://www.aviso.altimetry.fr). This is INCOIS contribution number 447.

Author contributions APA and MSG conceived the presented idea. APA performed the computations, data analysis, and interpretations of the result. MSG verified the methods. APA took the lead in preparing the first draft of the manuscript, and MSG led the finalization of the manuscript.

Funding None.

Availability of data and material Data availability and its source are stated in the manuscript and acknowledgement section.

Declarations

Conflict of interest The authors declare that they have no competing interests.

Consent to participate Agreed.

Consent for publication Agreed.

References

Ajayamohan RS, Rao AS (2008) Indian Ocean Dipole modulates the number of extreme rainfall events over India in a warming environment. J Meteorol Soc Jpn 86:245–252

Anderson SP, Weller RA, Lukas RB (1996) Surface buoyancy forcing and the mixed layer of the western Pacific warm pool: observations and 1D model results. J Clim 9:3056–3085

Ashin K, Girishkumar MS, Suprit K, Thangaprakash VP (2019) Observed upper ocean seasonal and intraseasonal variability in the Andaman Sea. J Geophys Res Oceans 124:6760–6786. https://doi.org/10.1029/2019JC014938

Ashok K, Guan Z, Yamagata T (2001) Impact of the Indian Ocean Dipole on the relationship between the Indian Monsoon Rainfall and ENSO relationship. Geophys Res Lett 28(23):4499–4502. https://doi.org/10.1029/2001GL013294

Ashok K, Guan Z, Saji NH, Yamagata T (2004) Individual and combined influences of ENSO and the Indian Ocean dipole on the Indian summer monsoon. J Clim 17:3141–3155

Atlas R, Hoffman RN, Ardizzone J, Leidner SM, Jusem JC, Smith DK, Gombos D (2011) A cross-calibrated, multiplatform ocean surface wind velocity product for meteorological and oceanographic applications. Bull Am Meteorol Soc 92:157–174. https://doi.org/10.1175/2010BAMS2946.1

AVISO Altimetry (2009) SSALTO/DUACS user handbook: (M)SLA and (M)ADT near-real time and delayed time products. Rep. CLS-DOS-NT-06.034, p 51. Ramonville-Saint-Agne, France

Behera SK, Yamagata T (2003) Influence of the Indian Ocean Dipole on the Southern Oscillation. J Meteorol Soc Jpn 81(1):169–177

Behera SK, Krishnan R, Yamagata T (1999) Unusual ocean–atmosphere conditions in the tropical Indian Ocean during 1994. Geophys Res Lett 26:3001–3004

Carton JA, Chepurin GA, Chen L (2018) SODA3: a new ocean climate reanalysis. J Clim 31(17):6967–6983. https://doi.org/10.1175/JCLI-D-18-0149.1

Delman AS, Sprintall J, McClean JL, Talley LD (2016) Anomalous Java cooling at the initiation of positive Indian Ocean Dipole events. J Geophys Res Oceans 121:5805–5824. https://doi.org/10.1002/2016JC011635

Delman AS, McClean JL, Sprintall J, Talley LD, Bryan FO (2018) Process-specific contributions to anomalous Java mixed layer cooling during positive IOD events. J Geophys Res Oceans 123:4153–4176. https://doi.org/10.1029/2017JC013749

Du Y, Qu T, Meyers G, Masumoto Y, Sasaki H (2005) Seasonal heat budget in the mixed layer of the southeastern tropical Indian Ocean in a high-resolution ocean general circulation model. J Geophys Res 110:C04012. https://doi.org/10.1029/2004JC002845

Fairall CW, Bradley EF, Hare JE, Grachev AA, Edson JB (2003) Bulk parameterization of air-sea fluxes: updates and verification for the COARE algorithm. J Clim 16:571–591

Foltz GR, McPhaden MJ (2009) Impact of barrier layer thicknesson SST in the central tropical North Atlantic. J Clim 22:285–299. https://doi.org/10.1175/2008JCLI2308.1

Forget G, Campin JM, Heimbach P, Hill CN, Ponte RM, Wunsch C (2015) ECCO version 4: an integrated framework for non-linear inverse modelling and global ocean state estimation. Geosci Model Dev 8:3071–3104. https://doi.org/10.5194/gmd-8-3071-2015

Gadgil S, Vinayachandran PN, Francis PA, Gadgil S (2004) Extremes of the Indian summer monsoon rainfall, ENSO and equatorial Indian Ocean oscillation. Geophys Res Lett. https://doi.org/10.1029/2004GL019733

Gentemann CL, Wick GA, Cummings J, Bayler E (2004) Multisensor improved sea surface temperature (MISST) for GODAE. In: Paper presented at 13th conference on satellite meteorology and oceanography, 19–23 Sept. 2004, Norfolk. at:http://www.remss.com/papers/gentemann/gentemann_13satmet_2004.pdf)

Girishkumar MS, Ravichandran M (2012) The influences of ENSO on tropical cyclone activity in the Bay of Bengal during October–December. J Geophys Res Oceans 117:C02033. https://doi.org/10.1029/2011JC007417

Girishkumar MS, Ravichandran M, Pant V (2011) Observed chlorophyll-a bloom in the southern Bay of Bengal during winter 2006–2007. Int J Remote Sens. https://doi.org/10.1080/01431161.2011.563251

Girishkumar MS, Ravichandran M, Han W (2013a) Observed intraseasonal thermocline variability in the Bay of Bengal. J Geophys Res Oceans 118:3336–3349. https://doi.org/10.1002/jgrc.20245

Girishkumar MS, Ravichandran M, McPhaden MJ (2013b) Temperature inversions and their influence on the mixed layer heat budget during the winters of 2006–2007 and 2007–2008 in the Bay of Bengal. J Geophys Res Oceans 118:2426–2437. https://doi.org/10.1002/jgrc.20192

Girishkumar MS, Joseph J, Thangaprakash VP, Pottapinjara V, McPhaden MJ (2017) Mixed layer temperature budget for the northward propagating Summer Monsoon Intraseasonal Oscillation (MISO) in the Central Bay of Bengal. J Geophys Res Oceans 122:8841–8854. https://doi.org/10.1002/2017JC013073

Horii T, Masumoto Y, Ueki I, HaseH MK (2009) Mixed layer temperature balance in the eastern Indian Ocean during the 2006 Indian Ocean dipole. J Geophys Res 114:C07011. https://doi.org/10.1029/2008JC005180

Horii T, Ueki I, Ando K, Mizuno K (2013a) Eastern Indian Ocean warming associated with the negative Indian Ocean dipole: a case study of the 2010 event. J Geophys Res Oceans 118:536–549. https://doi.org/10.1002/jgrc.20071

Horii T, Ueki I, Ando K (2013b) Contrasting development and decay processes of Indian Ocean Dipoles in the 2000s. Sci Online Lett Atmos 9:183–186. https://doi.org/10.2151/sola.2013-041

Izuka S, Matsuura T, Yamagata T (2000) The Indian Ocean SST dipole simulated in a coupled general circulation model. Geophys Res Lett 27:3369–3372

Izumo T, Vialarad J, Lengaigne M, de Boyer MC, Behera SK, Luo JJ, Cravatte S, Masson S, Yamagata T (2010) Influence of the state of the Indian Ocean Dipole on the following years El Nino. Nat Geosci 3(3):168–172. https://doi.org/10.1038/NGEO)760

Jha RK, Udaya Bhaskar, TVS (2020) Data-interpolating variational analysis (DIVA) method for the generation of argo data gridded products. Technical Report ESSO-INCOIS-TPG-TR01(2020). Indian National Centre for Ocean Information Services, Hyderabad, pp 1–46

Jiang X, Zhang T, Tam C-Y, Chen J, Lau N-C, Yang S, Wang Z (2019) Impacts of ENSO and IOD on snow depth over the Tibetan Plateau: roles of convections over the western North Pacific and Indian Ocean. J Geophys Res Atmos 124:11961–11975. https://doi.org/10.1029/2019JD031384

Kurian J, Vinayachandran PN (2006) Formation mechanisms of temperature inversions in the southeastern Arabian Sea. Geophys Res Lett 33:L17611. https://doi.org/10.1029/2006GL027280

Liebmann B, Smith CA (1996) Description of a complete (interpolated) outgoing longwave radiation dataset. Bull Am Meteorol Soc 77:1275–1277

Mareta L, Hidayat R, Hidayati R, Alsepan G (2018) Influence of the positive Indian Ocean Dipole in 2012 and El Niño-southern oscillation (ENSO) in 2015 on the Indonesian Rainfall Variability. IOP

Conf Ser Earth Environ Sci 284:012018. https://doi.org/10.1088/1755-1315/284/1/012018

McPhaden MJ (1982) Variability in the central equatorial Indian Ocean II, oceanic heat and turbulent energy balances. J Mar Res 40:403–419

McPhaden MJ, Hayes SP (1991) On the variability of winds, sea surface temperature, and surface layer heat content in the western equatorial Pacific. J Geophys Res Oceans 96:3331–3342

McPhaden MJ, Meyers G, Ando K, Masumoto Y, Murty VSN, Ravichandran M, Syamsudin F, Vialard J, Yu L, Yu W (2009) RAMA: the research moored array for African–Asian–Australian Monsoon analysis and prediction a new moored buoy array in the historically data-sparse Indian Ocean provides measurements to advance monsoon research and forecasting. Bull Am Meteorol Soc 90:459–480. https://doi.org/10.1175/2008BAMS2608.1

Morel A, Antoine D (1994) Heating rate within the upper ocean in relation to its bio-optical state. J Phys Oceanogr 24:1652–1665

Moum J, Perlin A, Nash J, McPhaden MJ (2013) Seasonal sea surface cooling in the equatorial Pacific cold tongue controlled by ocean mixing. Nature 500:64–67. https://doi.org/10.1038/nature12363

Murtugudde RG, Signorini SR, Christian JR, Busalacchi AJ, Mcclain CR, Picaut J (1999) Ocean color variability of the tropical Indo-Pacific basin observed by SeaWiFS during 1997–1998. J Geophys Res Oceans 104:18351–21836

Murtugudde R, McCreary JP, Busalacchi AJ (2000) Oceanic processes associated with anomalous events in the Indian Ocean with relevance to 1997–1998. J Geophys Res Ocean 105:3295–3306

Palmer TN, Mansfield DA (1984) Response of two atmospheric general circulation models to sea-surface temperature anomalies in the tropical east and west Pacific. Nature 310:483–488

Pant V, Girishkumar MS, Udaya Bhaskar TVS, Ravichandran M, Papa F, Thangaprakash VP (2015) Observed interannual variability of near-surface salinity in the Bay of Bengal. J Geophys Res Oceans 120:3315–3329. https://doi.org/10.1002/2014JC010340

Potemra JT, Lukas R, Mitchum GT (1997) Large-scale estimation of transport from the Pacific to the Indian Ocean. J Geophys Res Oceans 102:27795–27812

Praveen Kumar B, Vialard J, Lengaigne M, Murty VSN, McPhaden MJ (2012) TropFlux: air-sea fluxes for the global tropical oceans—description and evaluation. Clim Dyn 38:1521–1543. https://doi.org/10.1007/s00382-011-1115-0

Rao RR, Girishkumar MS, Ravichandran M, Rao AR, Gopalakrishna VV, Thadathil P (2010) Interannual variability of Kelvin wave propagation in the wave guides of the equatorial Indian Ocean, the coastal Bay of Bengal and the southeastern Arabian Sea during 1993–2006. Deep Sea Res Part I Oceanogr Res Pap 57(1): 1–13. https://doi.org/10.1016/j.dsr.2009.10.008 **(ISSN 0967-0637)**

Rao RR, Sivakumar R (2000) Seasonal variability of near-surface thermal structure and heat budget of the mixed layer of the tropical Indian Ocean from a new global ocean temperature climatology. J Geophys Res Oceans 105(C1):995–1015. https://doi.org/10.1029/1999JC900220

Ravichandran M, Behringer D, Sivareddy S, Girishkumar MS, Chacko N, Harikumar R (2013) Evaluation of the global ocean data assimilation system at INCOIS: the tropical Indian ocean. Ocean Model 69:123–135. https://doi.org/10.1016/j.oceramod.2013.05.003

Saji NH, Yamagata T (2003) Possible impacts of Indian Ocean dipole mode events on global climate. Clim Res 25(2):151–169

Saji NH, Goswamy BN, Vinayachandran PN, Yamagata T (1999) A dipole mode in the tropical Indian Ocean. Nature 401:360–363

Santoso A, Sengupta A, England MH (2010) Genesis of Indian Ocean mixed layer temperature anomalies: a heat budget analysis. J Clim 23(20):5375–5403. https://doi.org/10.1175/2010JCLI3072.1

Schott FA, Xie S-P, McCreary JP (2009) Indian Ocean circulation and climate variability. Rev Geophys 47:RG1002. https://doi.org/10.1029/2007RG000245

Sweeney C, Gnanadesikan A, Griffies S, Harrison M, Rosati A, Samuels B (2005) Impacts of shortwave penetration depth on large-scale ocean circulation heat transport. J Phys Oceanogr 35:1103–1119

Vinayachandran PN, Mathew S (2003) Phytoplankton bloom in the Bay of Bengal during the northeast monsoon and its intensification by cyclones. Geophys Res Lett 30(11):1572. https://doi.org/10.1029/2002GL016717

Vinayachandran PN, Kurian J, Neema CP (2007) Indian Ocean response to anomalous conditions in 2006. Geophys Res Lett 34:L15602. https://doi.org/10.1029/2007GL030194

Vinayachandran PN, Francis PA, Rao SA (2009) Indian Ocean Dipole: processes and impacts. Current trends in science. Indian Acad of Sci., Bangalore, pp 569–589

Wang G, Cai W (2020) Two-year consecutive concurrences of positive Indian Ocean Dipole and central Pacific El Nino preconditioned the 2019/2020 Australian "black summer" bushfires. Geosci Lett 7:19. https://doi.org/10.1186/s40562-020-00168-2

Wang G, Cai W, Yang K, Santoso A, Yamagata T (2020) A unique feature of the 2019 extreme positive Indian Ocean Dipole event. Geophys Res Lett 47:e2020GL088615. https://doi.org/10.1029/2020GL088615

Webster PJ, Moore AM, Loschnigg JP, Leben RR (1999) Coupled ocean-atmosphere dynamics in the Indian Ocean during 1997–98. Nature 401:356–360. https://doi.org/10.1038/43848

Wielicki BA, Barkstrom BR, Harrison EF, Lee RB III, Smith GL, Cooper JE (1996) Clouds and the Earth's Radiant Energy System (CERES): an earth observing system experiment. Bull Am Meteorol Soc 77:853–868. https://doi.org/10.1175/1520-0477(1996)077%3c0853:CATERE%3e2.0.CO;2

Yu L (2003) Variability of the depth of the 20°C isotherm along 6°N in the Bay of Bengal: its response to remote and local forcing and its relation to satellite SSH variability. Deep Sea Res 50:2285–2304

Yu L, O'Brien JJ, Yang J (1991) On the remote forcing of the circulation in the Bay of Bengal. J Geophys Res 96:20449–20454

Zhang L, Du Y, Cai W (2018a) Low-frequency variability and the unusual Indian Ocean Dipole events in 2015 and 2016. Geophys Res Lett 45:1040–1048. https://doi.org/10.1002/2017GL076003

Zhang L, Du Y, Cai W (2018b) A spurious positive Indian Ocean Dipole in 2017. Sci Bull 63(18):1170–1172. https://doi.org/10.1016/j.scib.2018.08.001

Publisher's Note Springer Nature remains neutral with regard to jurisdictional claims in published maps and institutional affiliations.